IRAQI BULLETIN OF GEOLOGY AND MINING (IBGM)\
IRAQ GEOLOGICAL SURVEY (GEOSURV-IRAQ)

*IBGM (**2025**, Vol 21; Issue 2)* *505-544*

GEOCHEMICAL AND MORPHOLOGICAL CHARACTERISTICS OF THE HALGURD PILLOW BASALTS: EVIDENCE FOR BACK-ARC MAGMATISM IN THE ZAGROS SUTURE ZONE OF KURDISTAN REGION, OF NORTHEAST IRAQ

Shaheen Ali Shaheen[1*], Mohammad Pirouei[2], and Yousif Osman Mohammad[2]

[1] Petroleum Geoscience, Faculty of Science, Soran University, e-mail: shahen.shahen@Soran.edu.iq; mohammad.askandar@Soran.edu.iq
[2] Department of Geology, Sulaimani University, e-mail: Yousif.mohammad@Univsul.edu.iq
***** Correspondence: shahen.shahen@Soran.edu.iq; Shaheen Ali Shaheen

Type of the Paper (Article)
Received: 20/09/2025
Revised: 20/10/2025
Available online: 27/12/2025

Abstract

The Halgurd volcanic-dominated mountain, situated near the Iranian border, is the highest peak within the Zagros Orogenic Belt in the Kurdistan region of northeast Iraq, reaching an elevation of 3,607 meters above sea level. Field observations reveal that its complex structure bears a resemblance to an ophiolite, comprising sedimentary and metasomatic rocks, thin intrusive serpentinite, and gabbroic and mafic sheets at the mountain base, overlain by a thick sequence of mafic lava and pillow basalts that form the mountain cap. This study focuses on the Halgurd Pillow Basalt (HPB), using morphometric, petrological, geochemical, and mineralogical analyses. Field data suggest that the pillows were emplaced in a shallow-water basin with gentle slopes under rapid cooling conditions. Geochemical analysis reveals a moderately TiO_2 content (1.5 – 2.1 wt.% %) and La/Yb_n ratios (1.83 – 4.37), as well as significant enrichment in light rare earth elements (LREE) relative to heavy rare earth elements (HREE), with characteristics of a tholeiitic magma series. The HPB also displays pronounced negative Nb and Ta anomalies, as well as elevated Th/Yb ratios, which indicate a subduction-modified mantle source, consistent with back-arc basin magmatism. Relative to the primitive mantle, HPB samples are moderately depleted in Cr (182 – 343 ppm) and Ni (53 – 96 ppm) and exhibit a negative Y anomaly, suggesting the fractionation of spinel, olivine, and amphibole. Based on pillow morphology, geochemical discrimination diagrams, and Ti/V ratios, the HPB is interpreted to have formed in a relatively deep back-arc basin setting with affinities to enriched mid-ocean ridge basalt (E-MORB) magmatism.

Keywords: Back-Arc; Halgurd; Ophiolite; Pillow Basalt; Tholeiitic.

ISSN 1811-4539, EISSN 3005-3714
https://doi.org/10.59150/ibgm2102a28
IBGM: http://ibgm-iq.org/
Academic Scientific Journals: www.iasj.net

1. Introduction

Pillow basalts form as a result of the rapid cooling of lava upon contact with a water body, where the significant temperature contrast between lava and water creates tongue-like outer skins that develop into characteristic pillow structures. As lava continues to fill the interior of the tongue, it expands into a lobe. Once internal pressure builds sufficiently, it ruptures the solidified outer skin, producing a new eruption point near the original vent (Martí et al., 2005). The preservation of pillow lavas has also been documented in older volcanic sequences, including some subglacial volcanoes during the initial stages of eruption (Tronnes, 2002). As key features of the uppermost sections of ophiolite complexes, pillow lavas offer valuable insights into the nature of the parent magma, the degree of partial melting, and the paleotectonic setting of the region (Dilek & Newcomb, 2003; Duncan et al., 1987; Langdon, 1982).

Not all submarine lava flows produce pillow structures; the formation of pillow lavas versus sheet flows largely depends on the lava emission rate. Experimental data and field observations indicate that moderate flow rates of basaltic lava favor the development of tubular pillow lavas, whereas higher flow rates result in ponded or pillar-like sheet flows with distinctly different morphologies (Chadwick, Jr, & Embley, 1994; Fink & Griffiths, 1990). Since flow rate is directly influenced by melt viscosity, variations in viscosity lead to dramatically different lava morphologies on the seafloor. According to several models, lava with a viscosity corresponding to a discharge rate of less than 1 m^3/s typically forms pillows; flow rates between 1 – 100 m^3/s produce lobate sheets; 100 – 3,000 m^3/s result in ropy sheet flows; and rates exceeding 3,000 m^3/s give rise to jumbled sheet flows (Griffiths & Fink, 1992). The intermediate to high effusion rates commonly observed at mid-ocean ridges have led to the formation of complex sequences of submarine volcanic rocks, comprising alternating layers of sheet flows, lava lakes, and pillow lavas distributed across space and time on the modern ocean floor (Juteau, 1993; Kennish & Lutz, 1998). Additionally, transitions from lava lakes or sheet flows into pillow lavas may occur when effusion rates decrease to moderate levels (Griffiths & Fink, 1992).

When lava comes into contact with standing water, a variety of morphological forms can develop. The most common include equidimensional, blob-like structures, as well as elongate and tongue-shaped features (Winter, 2010). These morphological characteristics have also been widely used to infer the physicochemical conditions of the seafloor at the time of lava emplacement, such as basin depth and slope (Martíet al., 2005). Furthermore, the chemical composition of the lava can often be inferred from pillow morphology—particularly their diameters. For example, the largest pillows are typically composed of olivine-rich tholeiitic basalt, followed by medium-sized pillows of andesite, whereas smaller pillows have tholeiitic and basaltic composition (Fridleifsson et al., 1982).

Pillow lavas have been extensively studied worldwide as key indicators of submarine volcanic activity. They serve as important markers for understanding paleotectonic processes, including seafloor spreading mechanisms, the reconstruction of paleo-oceanic environments, the evolution of oceanic crust, and the dynamics of lava eruption and cooling rates (Ahmad et al., 2024; Al-Qayim et al., 2012; Aswad et al., 2013; Boniface & T. Tsujimori, 2019; Farahmand

& Arian, 2014; Qaradaghi et al., 2019; Ramsay & Moore, 1985; Ural et al., 2015; L. Q. Xia et al., 2016).

The primary objective of this investigation is to document the petrogenesis, the depth and degree of partial melting of parental rock from which Halgurd Pillow Basalt (HPB) originated, as well as the assessment of tectonic setting, and reconstruction of the geodynamic model for the study area. This is achieved through an integrated analysis of mineralogical, geochemical, petrological, and morphological data. Additionally, the study places particular emphasis on the morphology of pillow lavas as a means to infer the approximate depth of the subaqueous environment in which pillows are formed, the slope of lava emplacement, and the cooling rate of lava.

1.1. Tectonic and regional geology

The investigated area is situated within the Halgurd Mountain range, recognized as the highest mountain in the whole Iraqi territory. Its peak reaches 3607 m above sea level, belonging to Choman district, about 170 Km northeast of Erbil Province and 57 Km northeast of Soran city, Kurdistan region of northeast Iraq. The Iraqi territory, including the Kurdistan region, has been divided into four tectonic zones: Foothill, High Folded, Imbricated, and Suture Zones (Figure 1a). The suture zone, which stretches throughout the extreme northeastern part of Iraq, is broadly classified into three major segments: The Qulqula-Khwakurk, Penjween-Walash, and Shalair zones (Goff & Jassim, 2006).

The Halgurd igneous complex is dominated by mafic volcanic and intrusive sheets, serpentinite bodies, and chert layers. This complex in the vicinity of the Hasanbag arc is positioned within the Zagros Orogenic Belt (ZOB), formally known as Zagros Fold–Thrust Belt in the northeast of Iraq. This belt is tectonically situated between the Sanandaj-Sirjan Zone (SSZ) and the Arabian shield (S. A. Ali et al., 2019), formed during the Late Cretaceous to Cenozoic Arabia-Eurasia collision (Abdulrehman et al., 2023; Mouthereau et al., 2012) and is considered an extensive part of the approximately 2000 km long Alpine-Himalayan Mountain Range, undergoing drastic deformation in the vicinity of the Iraq-Iran border (Alavi, 1994; Othman & Gloaguen, 2013; Ali et al., 2019). The belt is built up from the ongoing long-span collision between the Eurasian and Arabian plates (Fouad, 2014) through three significant tectonic events: subduction, obduction, and collision during the early Cretaceous to Cenozoic (Moghadam et al., 2019; Ali, 2012; Ali et al., 2012,2013). Reconstruction of paleotectonic components in the NW Zagros suture zone includes mantle plume, subduction zones, multiple tectonic domains, and lithostratigraphic successions of suture zones along the collision zone (Azizi et al., 2013; Moghadam et al., 2020). However, due to the complex evolution of the convergence history, multiple collision timeframes have been suggested for the collision with a minimum inferred age assigned to the Late Oligocene (Koshnaw et al., 2019).

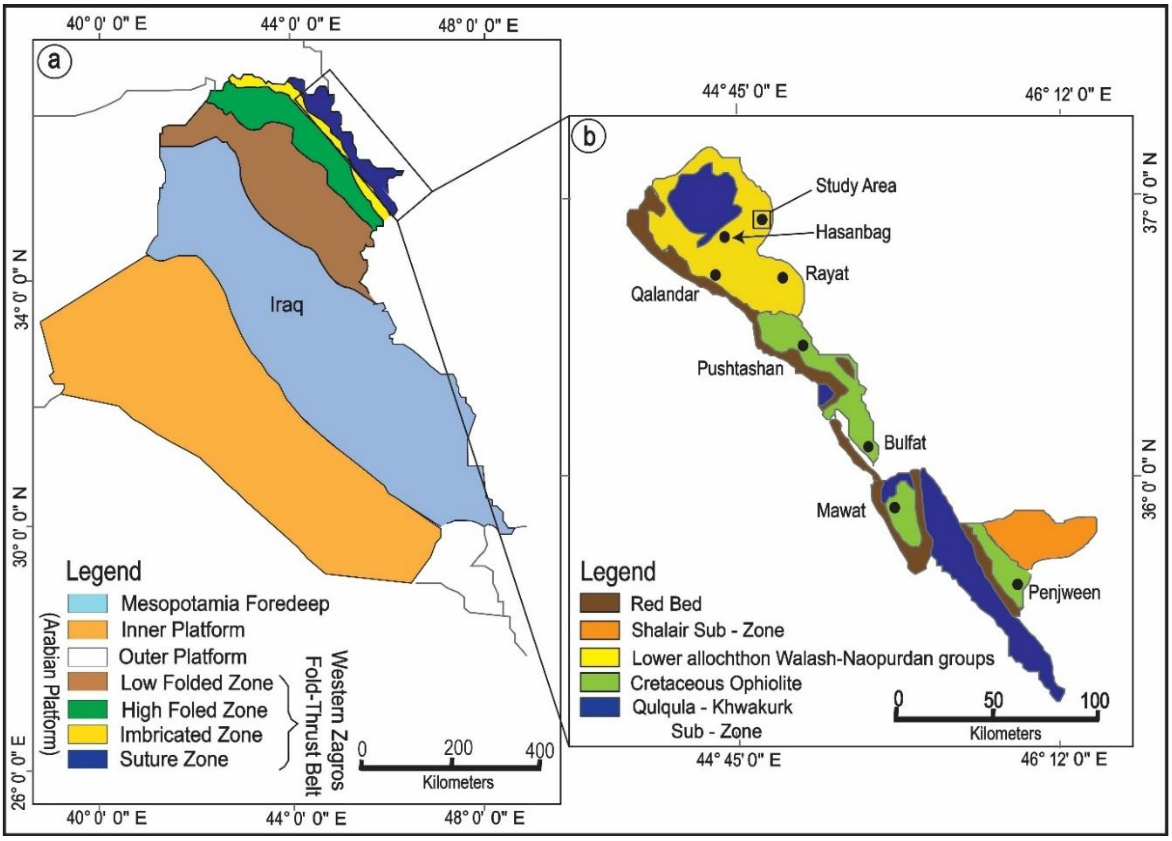

Figure 1. The tectonic framework of Iraq demonstrates the major structural zones that constrain the distribution of lithological units and deformation patterns, highlighting the Suture tectonic zone, including the study area and other neighboring ophiolite complexes. (a) The distribution of tectonic zones on the Iraq map displays the location of the study area in the Zagros Suture Zone (modified after *Fouad, 2015; Goff & Jassim, 2006; Sissakian, 2013)*(b) location of the study area on the detailed map of the Iraqi Zagros Suture Zone, modified by Buday (1975).

The Zagros Fold – Thrust Belt in Iraq is tectonically divided into 1) the Inner Platform (Stable Shelf) and 2) the Outer Platform (Unstable Shelf). The Mesopotamia Foredeep and the Western Zagros Fold-Thrust Belt are the subdivisions of the Outer Platform (Unstable Shelf) (Fouad, 2015; Goff & Jassim, 2006). The Western Zagros Fold-Thrust Belt includes four subzones: the Low Folded Zone, High Folded Zone و Imbricated Zone (IZ), and the Zagros Suture Zone (ZSZ) (Figure 1a; Agard et al., 2011; Fouad, 2015; Goff & Jassim, 2006; Lawa et al., 2013; Othman & Gloaguen, 2013). The Suture Zone is subdivided into the Qulqula-Khwakurk radiolarite, the Penjween-Walash, and the Volcano-sedimentary Shalair zone (Jassim and Goff 2006). According to this classification, the study area is situated within the Penjween-Walash subzone (Figure 1b).

The Penjween-Walash subzone that builds up the center of Neo-Tethys is composed of the sequences of volcanic-sedimentary rocks formed as a consequence of Neo-Tethys seafloor spreading during the Cretaceous, Paleogene syn-tectonic evolution, and arc volcanic activities associated with basic intrusive rocks during the last stage of ocean closure (S. A. Ali et al., 2019; Mohammad et al., 2023). This subzone thrusts over the Balambo-Tanjero or Qulqula-Khwakurk zones. The Cretaceous sequence comprises pelitic, carbonate, extrusive, and pyroclastic rocks and has undergone metamorphism and deformation processes during the Late Cretaceous, forming a voluminous mass about 400 m thick. However, the Paleogene succession comprises two units; the internal unit consists of volcanic rocks (andesite, basalt, and acidic rocks), and the outer unit is dominated by flysch volcanic rocks (Goff & Jassim, 2006).

The Penjween-Walash subzone encompasses the upper and lower allochthonous thrust sheets. The lower allochthonous represents the Walash-Naopurdan Groups, whereas the upper allochthonous is built of ophiolite-bearing terrane (K. J. Aswad et al., 2011; Aziz et al., 2011; Mohammad et al., 2014; Mohammad & Cornell, 2017). The investigated area from the Halgurd Mountain is associated with the Walash-Naopurdan Groups Figure (2a & b). The group is dominated by a volcanic-sedimentary sequence (Ali & Rostum, 2021; Goff & Jassim, 2006) that endured regional metamorphism, and based on the feldspar ^{40}Ar–^{39}Ar and Zircon U-Pb analysis for the magmatic rocks, the Late Cretaceous - Oligocene age is suggested for the Walash Volcanic Rocks (Aswad et al., 2013; Mohammad et al., 2023).

2. Materials and methods

Following extensive field observations and in-situ rock identification, 20 representative hand samples of pillow basalts, sheeted dyke basalt, altered rocks, gabbro, and serpentinite were systematically collected for petrographic, geochemical, and mineralogical analyses. Each sample was GPS-referenced and labeled in the field to ensure spatial accuracy and to support the construction of the geological map depicting the distribution of the studied rock units.

Multiple analytical techniques and instruments were employed, including petrographic microscopy, X-ray diffraction (XRD), and inductively coupled plasma–mass spectrometry (ICP-MS). Thin sections were prepared and examined under both transmitted and reflected light microscopes for detailed textural and mineralogical identification.

Silver-coated thin-polished sections were analyzed using Scanning Electron Microscopy with Energy Dispersive X-ray Spectroscopy (SEM-EDS). These analyses were conducted at the Scientific Research Center, Soran University (Kurdistan Region, Iraq), using a BRUKER-QUANTAX EDS system with an FEI 480 SEM at 15 – 25 kV accelerating voltage, 1 – 2 µm beam size, 20 nA beam current, and 25-second count time.

Besides optical microscopy studies, mineral phases and their approximate proportions were determined using XRD with a Philips Panalytical X’Pert PRO MPD Alpha powder diffractometer, set in Bragg-Brentano θ/2θ geometry (240 mm radius), using Cu-filtered Kα radiation (λ = 1.5418 Å) at 40 mA and 45 kV. These analyses were also performed at the Scientific Research Center, Soran University.

Whole-rock geochemical analyses were carried out at Zarazma Mineral Studies Company (Iran) using XRF and ICP-MS techniques for major and trace element quantification, respectively. Before analysis, samples were fused with lithium borate and dissolved in nitric acid. The loss on ignition (LOI), representing volatile and hydrous components in the samples, was measured by heating one gram of powdered sample at 950°C for 2 hours in a Selecta® muffle furnace.

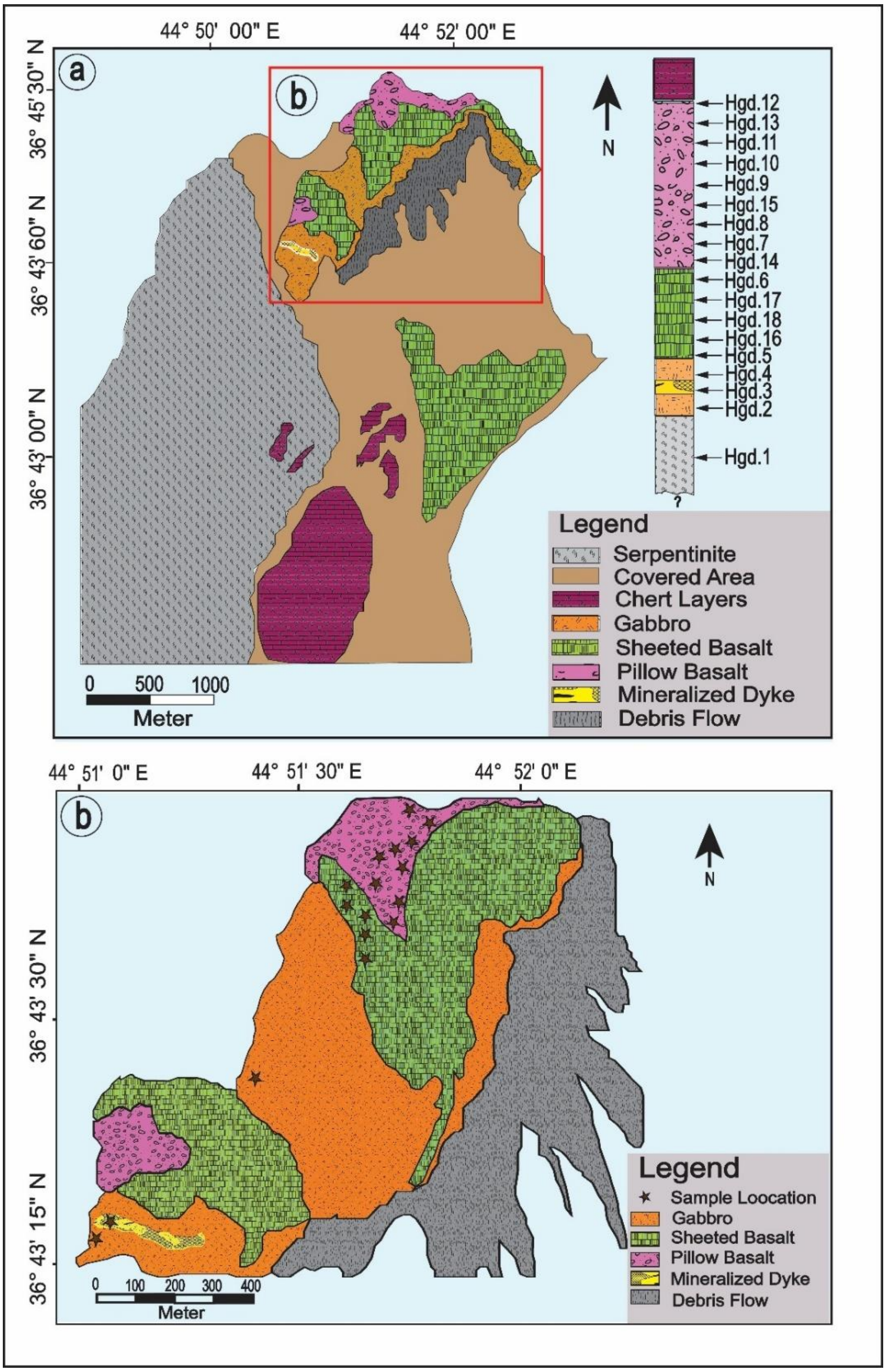

Figure 2. a) Regional geological map of Halgurd Mountain illustrates the spatial relationship between the investigated area and the associated lithological units, including gabbro, chert layers, and serpentinite. b) Detailed geological map exhibits the study area and the distribution of associated rocks with marked points of the collected rock specimens, as presented by the red cubic outline in panel (a).

3. Results

3.1. Field observations and rock identification

Due to the absence of a detailed geological map—largely a result of past political instability in the tri-border region of Iraq, Iran, and Turkey, where the study area is located—except for a general map at a 1/250000 scale, no official detailed geological mapping has been conducted in previous decades. To address this gap, extensive fieldwork was carried out to observe, record, and classify the lithological units in their natural context. Detailed geological mapping and on-site rock identification were performed to analyse the spatial relationships, structures, textures, and mineral compositions of the exposed rocks. Special focus was given to identifying pillow basalts and related lithologies, which were thoroughly examined based on their morphology, field setting, and surface characteristics.

Halgurd Mountain's rugged terrain is characterized by three primary rock types: predominantly igneous, moderately sedimentary, and less commonly metamorphic. Their spatial distribution reflects the region’s complex tectonic history, including both formation and deformation processes. The mountain’s foothills are mainly composed of tectonic slices containing sandstone, chert layers, and serpentinite. In contrast, the steeper slopes and summit are dominated by exposures of gabbro, sheeted basalt, and pillow basalt. A detailed description of these rock units follows.

3.1.1. Serpentinite

The gray-greenish, massive serpentinite units are prominently exposed along the slopes and faces of Halgurd Mountain, predominantly forming the mountain’s basal section. However, due to erosion and surface runoff, serpentinite exposures have also extended onto the steeper slopes (Figure 3a). A distinctive feature of this unit is the presence of intense foliation, indicative of ductile deformation. Additionally, the rocks show extensive brittle deformation, manifested by numerous fractures, although serpentine polymorph vein development is notably absent.

3.1.2. Gabbro

This unit is characterized by its distinctive layered structure (Figure 3b). Surface weathering processes, especially oxidation, have resulted in dark brown coloration and smooth rock surfaces. Gabbro is heavily fractured and intensely weathered, which makes it easier to distinguish from basalt sheets, whose identification is more challenging due to their similar external features. Many of the fractures in gabbro are partially infilled with epidote–chlorite veins. The rock is mostly medium-grained, though small-scale compositional layering is evident due to moderate to high alteration. Occasionally, large-grained or pegmatitic textures are also observed (Figure 3c).

3.1.3. Sheeted basalt

The sheeted basalts are characterized by steeply dipping cliffs and a color range from yellow to dark brown, with occasional brecciated zones (Figure 3d). Epidote–chlorite veins are common, and numerous fractures are filled with quartz, due to hydrothermal fluid circulation. While large phenocrysts are absent, amygdules are frequently observed. Structural differences between the sheeted and pillow basalts create a clear boundary between the two units Figure 3e. This unit also includes chert interlayers and lenses (Figure 3f). The presence of these chert inclusions is likely due to the collapse of chert fragments into flowing lava, followed by rapid cooling before complete melting could occur.

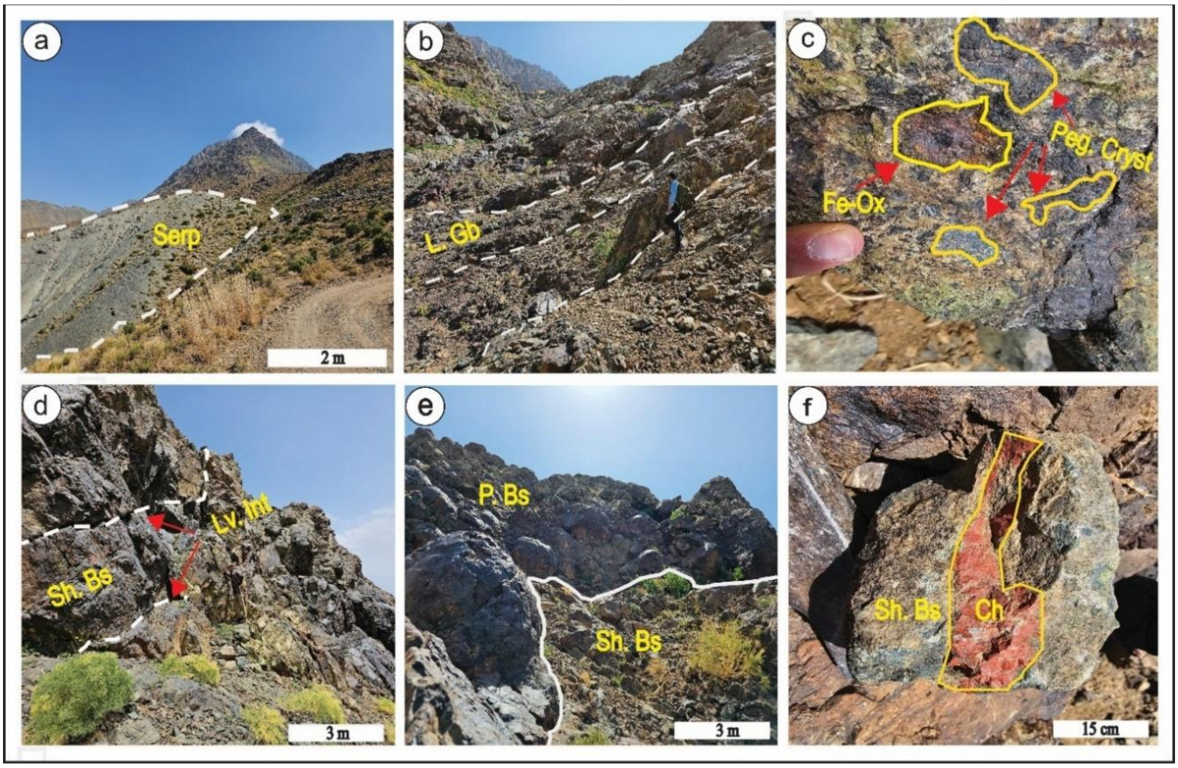

Figure 3. Field exposure of serpentinite, gabbro, sheets and pillow basalts from Halgurd Mountain area a) the steep slope appearance on surface body of serpentinite rocks due to severe erosion, b) Layered gabbro demonstrating magmatic stratification through several subsequent magmatic episodes, c) pegmatite crystals and oxidized sulfide phase in gabbro indicate the magmatic and post-magmatic processes in the host rocks, d) outcrop view of sheeted basalts showing subparallel dikes, e) the contact between sheeted basalts and pillow basalts, the sheeted basalts are relatively highly weathered with comparison to massive pillow basalt and f) sheeted basalt with chert inclusion (Serp: serpentinite, L. Gb: Layered gabbro, Fe-Ox: Iron oxide, Peg. Cryst: Pegmatite crystals, Sh. Bs: sheeted basalt, Ch: chert, and P. Bs: pillow basalt).

3.1.4. Pillow basalts (Pillow morphology)

The loosely to semi-tightly packed pillow basalts are prominently exposed above the sheeted basalt, particularly along the slopes and ridges of Halgurd Mountain (Figure 4a & b). Despite weathering and tectonic deformation, the pillows have retained their original morphology remarkably well. Surface oxidation has imparted a dark brown color and smoothed texture, occasionally cross-cut by quartz and epidote veins (Figure 4c & d). The pillow structures are described based on several physical characteristics, including the degree of packing, size and shape, chilled margins, vesicles, cavities, shell-like structures, concentric cracks, and radial contraction joints—many of which are visible in cross-sectional views. These pillows are also distinguished by well-developed "bread crust" cracking patterns on their outer surfaces (Figure 4c).

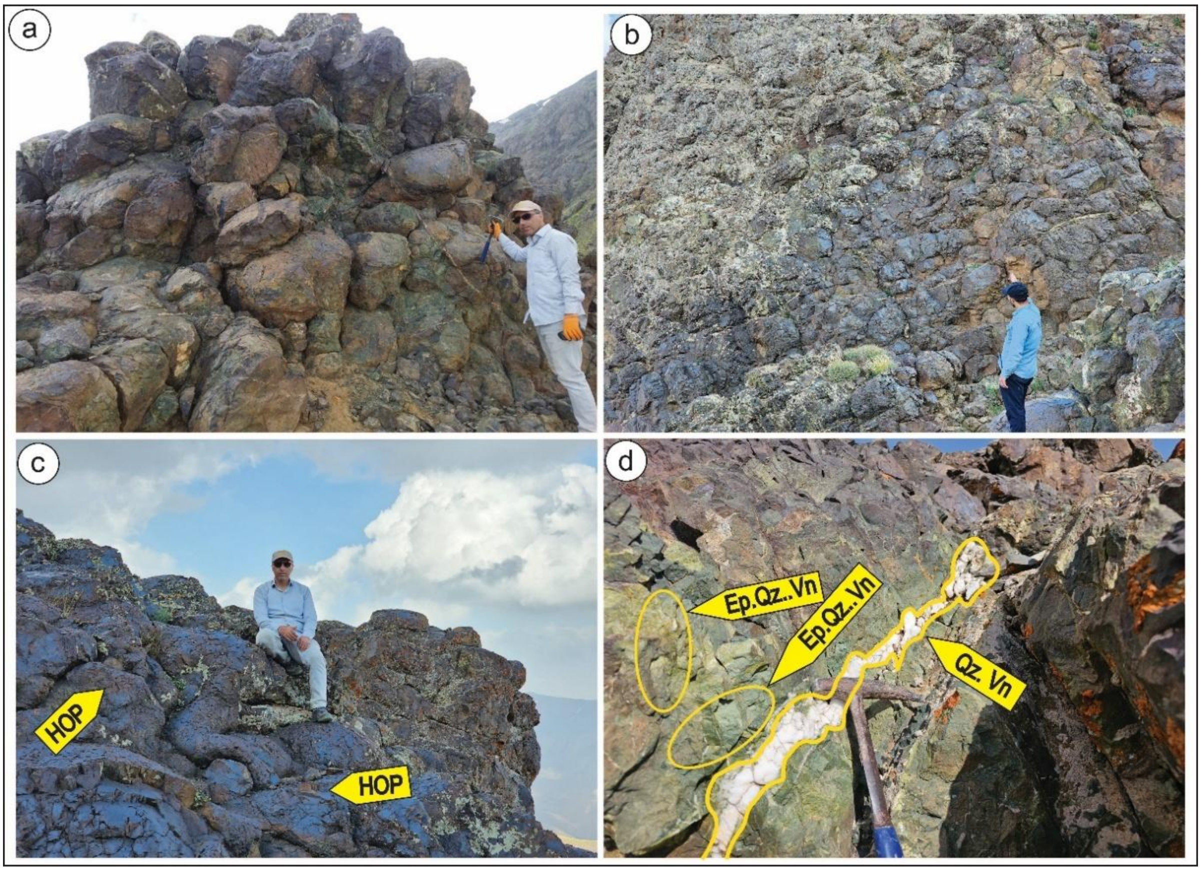

Figure 4. pillow basalts from outcrops of field study showing two major types of packing and the common veins, and morphological features dominated in the exposed rock: a) schematic view of pillows show loosely packed pattern with abundant inter-pillow materials and wide spaces b) semi-tightly packed profile of pillows with small volume of inter-pillow components c) the pillow surfaces displaying the movement of lava flow and dark brown color due to highly oxidization and d) the abundance of epidote and quartz vein in pillow bodies, vary in size from a few millimeter to several centimeter thick (HOP: highly oxidized pillows, Ep. Qz. Vn: epidote and quartz veins, and Qz. Vn: quartz vein).

The pillow lavas exhibit features such as concentric cracks, broad inter-pillow spaces, noticeable flattening, and a tubular shape (Figure 5a & b). Radial and concentric cracks show mild distortion and appear wavy, typically filled with quartz and epidote. The pillows also display chilled, glassy rims with aphanitic textures (Figure 5c & d). Convex, V-up structures in the 3D pillow arrangement are clearly visible and serve as indicators of stratigraphic top and bottom (Figure 6a). The pillows are loosely arranged, with open gaps at their contacts, partially filled by secondary materials like quartz, epidote, chlorite, or remnants of solidified lava (Figure 6a, b, & c). Some spherical pillows feature cuspate bases, with cusps oriented perpendicular to the horizontal axis. Other notable features include shelf structures, vesicles, drainage cavities, and the small to medium rounded forms of the pillows, suggesting they are largely undeformed in the HPB (Figures 5d, 6a – c).

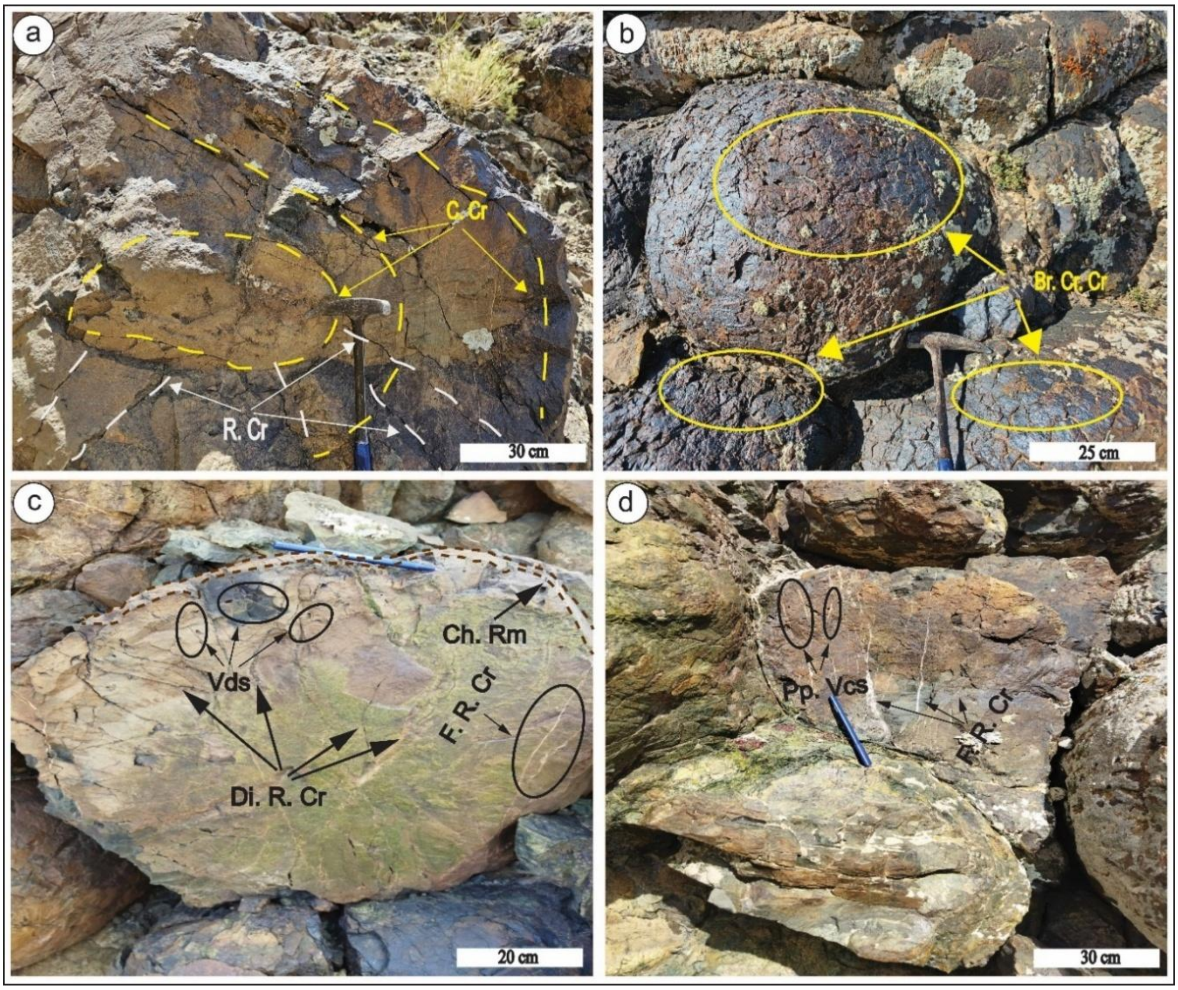

Figure 5. Morphological features of pillow basalts from field study area exhibit internal and external structures of pillows a) primary structures of pillows; regular concentric and radial cracks developed within pillows during the quenching of lava b) bread crust cracks on the pillow surfaces formed during the eruption of lava, upon contact with water body, due to rapid cooling c, d) internal view of a pillow demonstrates the inner and outer structures, such as distorted and filled radial cracks, voids, and chilled rims (where C. Cr: concentric cracks, R. Cr: radial cracks, Br. Cr. Cr: bread crust cracks, Di. R. Cr: distorted radial cracks, F. R. Cr: filled radial cracks, Vsd: voids, Pp. Vcs: pipe vesicles, and Ch. Rm: chilled rims.

Though loosely packed, some inter-pillow spaces contain significant amounts of chlorite and epidote, which appear as flakes due to alteration processes such as chloritization and epidotization (Figure 6a – c). Pillow morphology and size also vary depending on their tectonic setting, providing insights into environmental conditions (Ural, 2014). Pillow sizes range from small to large across different sections. Based on Walke's (1992a) classification, the HPB mainly contains normal pillows (<100 cm in length), with occasional mega pillows exceeding 100 cm, and some micro-pillows are also present (Figure 6).

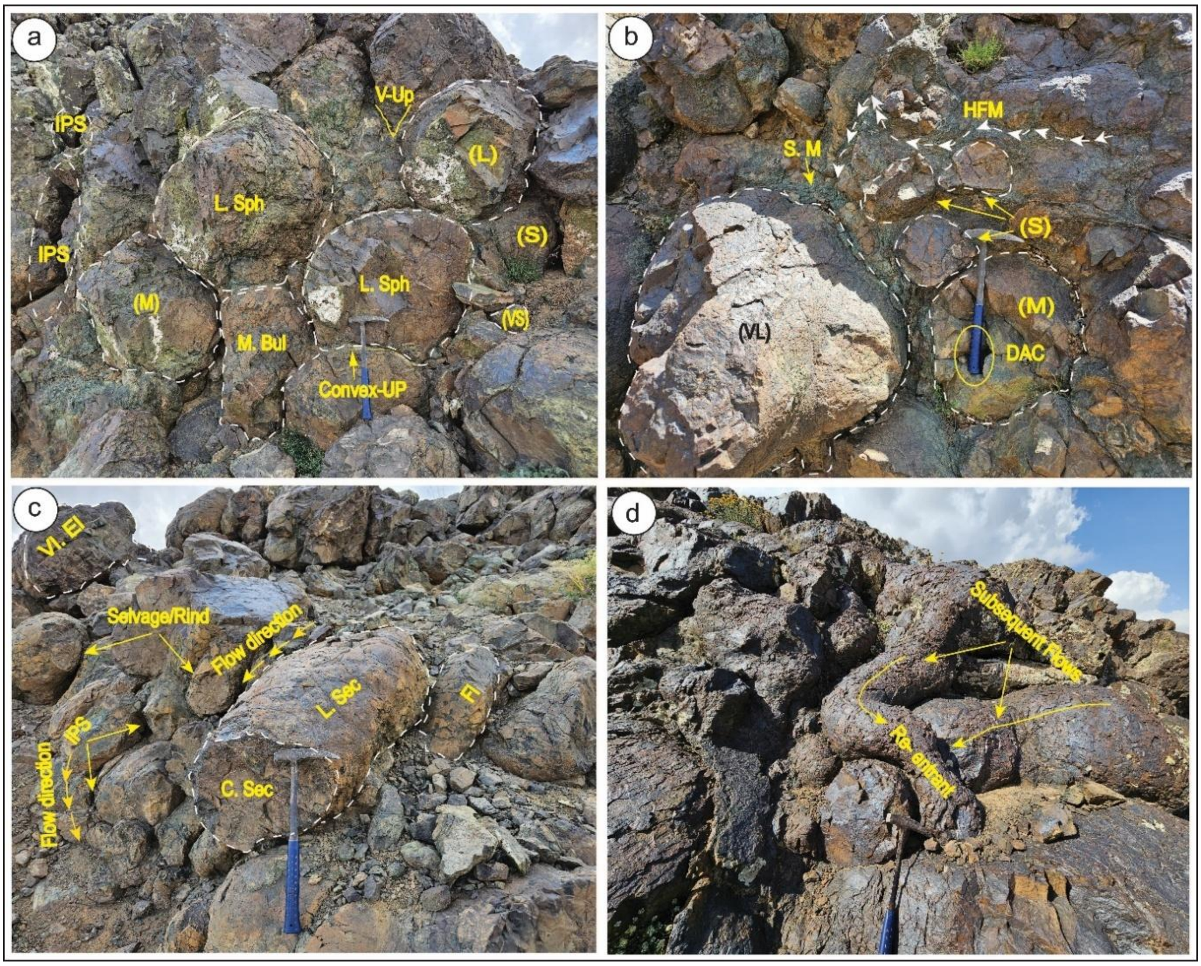

Figure 6. Morphological features of pillow in both cross and longitudinal sections a) cross-sectional view of pillows show pillows with diverse diameters, vary from very small to very large, the most common type is the normal size with various forms b) very large pillow separated from other types by a matrix, typically formed during the interaction of lava and water c) longitudinal section of pillows shows the arrangement of tubular pillows sub-parallel to the direction of lava flow and d) two subsequent of lava flows overpassed each other with re-entrant nature (where Vs: very small, S: small, M: medium, L: large, VL: very large, L. Sph: large spheroidal, M. Bul: Medium bulbous, HFM: hydrothermal fluid movement, DAC: drain away cavity, S.M: surface material, Vl. El: very large elliptical, Fl: flattened, IPS: inter-pillow spaces, L. Sec: longitudinal section, and C. Sec: cross section.

Analysis of longitudinal and cross-sectional profiles reveals that pillow shape is influenced by slope gradients at the time of emplacement. Common forms include spheroidal, elliptical, flattened, and bulbous pillows—seen in profile as elongated, tubular bodies with curving or inflected forms (Figure 6). Void development within HPB varies in size and shape. Small spherical and subspherical voids are widespread, mostly concentrated near pillow margins as isolated or connected vesicles, often aligned perpendicular to the chilled rims (Figure 5c & d).

Inter-pillow voids occur in various shapes—triangular, flattened, and irregular—sometimes partially filled with secondary minerals (Figure 6a). These spaces may enlarge due to rapid lava cooling or secondary mineral leaching during weathering. Additional void types include pipe vesicles and drain-away cavities (Figures 5d & 6b). Pipe vesicles, typically 5 – 10 cm long, are well-developed near the rims, sometimes radiating from the core. While large drain cavities are rare, smaller ones are common toward the center. Although many vesicles remain empty, cracks and inter-pillow gaps are often filled with quartz and epidote (Figures 5c, d, & 6b). Small amygdules, spherical, subspherical, irregular, or tubular, are frequently present throughout the pillow interiors.

3.2. Petrographic and XRD characteristics

Petrographic and XRD analysis (Table 1) indicates that the mafic rocks of the Halgurd region have experienced deformation and alteration under greenschist facies metamorphism. The following are the petrographic and XRD descriptions of the common rock types found in the Halgurd Mountain.

3.2.1. Pillow basalt

The most significant lithological unit in this study is the pillow basalts. Petrographic observations confirm the evidence of deuteric alteration, leading to the development of new mineral phases such as chlorite, dolomite, and epidote (Figure 7a). The primary mineral is plagioclase, which shows intense alteration to secondary albite and epidote. Pyroxene, the second most abundant mineral, is partially to completely replaced by chlorite, dolomite, and occasionally epidote.

Plagioclase shows high alteration with albite, andesine, and a minor amount of anorthite in compositions, ranging between (7.5 – 40.1 %), (4.3 – 22.8 %), and (0.1 – 0.2 %), respectively. Pyroxene occurs in the form of augite (9.6 – 28.4 %), enstatite (2.0 – 28.5 %), and diopside (2.7 – 12.8 %). Titanite participated as an accessory phase with a range between (3.2 – 9.9 %), other phases are quartz (2.5 – 6.6 %), epidote (0.5 – 2.2 %), magnetite (0.5 – 2.8 %), and hematite (0.5 – 2.4 %). Amygdules vary in shape (tubular, spheroidal, and rounded) and composition, being mostly filled with carbonate minerals and chlorite, with some containing fibrous epidote. Complex amygdules show syntaxial growth, with dolomite cores rimmed by chlorite and vice versa (Figure 7a).

The textural zoning of the pillow basalts includes: (i) outer rim: characterized by common fan- or sheaf-like clusters, set in a glassy to cryptocrystalline matrix (Figure 7b). Interstitial spaces are filled with granular orthopyroxene, opaque minerals, and abundant secondary alteration phases. (ii) middle zone: displays variolitic texture due to intergrowth of radial plagioclase and clinopyroxene, set in a matrix of plagioclase microlites, pyroxenes, opaque minerals, and minor glass (Figure 7c). Intergranular textures form networks of augite and chlorite grains between plagioclase laths. Amygdules in this zone include spherical composites with dolomite rims and chlorite cores. (iii) core zone: distinguished by holocrystalline texture, coarser grains, and less alteration (Figure 7d). The core zone is dominated by intergranular texture, with clinopyroxenes and opaque minerals occupying spaces between plagioclase laths. Plagioclase occurs as anhedral phenocrysts, up to 0.2 mm in length, often with inclusions and reaction rims (Figure 7d).

Table 1. X-ray diffraction (XRD) data presenting the contribution of mineralogical phases in Halgurd basaltic rocks and the associated paragenetic rocks, with a predominance of alteration minerals.

Sample	**Hgd.1**	**Hgd.3**	**Hgd.4**	**Hgd.5**	**Hgd.6**	**Hgd.8**	**Hgd.9**	**Hgd.11**	**Hgd.13**	**Hgd.14c**	**Hgd.14e**	**Hgd.14m**
Rock	**Serp**	**Epd**	**Gb**	**Al.Bs**	**Sh.Bs**	**P.Bs**	**P.Bs**	**P.Bs**	**P.Bs**	**P.Bs**	**P.Bs**	**P.Bs**
Albite	-	11.70	41.20	8.71	30.41	7.52	27.82	30.51	40.13	22.31	29.30	22.10
Andesine	-	2.60	13.20	0.30	8.30	22.80	4.30	10.30	7.20	16.40	11.10	18.00
Anorthite	-	-	2.30	-	0.91	-	-	-	-	-	0.21	0.11
Antigorite	63.20	-	-	-	-	-	-	-	-	-	-	-
Augite	-	-	-	9.70	24.01	24.60	13.81	9.60	14.20	28.41	26.51	19.20
chalcopyrite	-	-	-	0.51	0.61	-	-	-	-	-	-	-
Chlorite	-	-	-	21.01	20.71	28.40	17.50	22.40	14.70	17.10	20.61	21.40
Chromite	2.10	-	-	-	-	-	-	-	-	-	-	-
Chrysotile	29.20	-	-	-	-	-	-	-	-	-	-	-
Diopside	-	-	-	-	-	-	-	12.80	-	2.70	-	9.91
Dolomite	-	-	-	0.70	-	-	-	-	-	-	-	-
Enstatite	-	-	13.71	-	8.30	14.61	28.50	2.40	11.10	2.01	4.20	-
Epidote	-	35.80	6.41	21.50	1.10	0.51	1.31	2.20	0.51	1.01	-	-
Hematite	-	0.21	-	-	-	-	-	0.51	2.40	-	-	-
Hornblende	-	-	11.81	-	-	-	-	-	-	-	-	-
Ilmenite	-	-	-	-	-	-	-	-	0.71	-	-	-
Lizardite	4.01	-	-	-	-	-	-	-	-	-	-	-
Magnetite	1.61	-	-	-	2.31	-	-	2.81	0.81	-	0.51	0.60
quartz	-	49.80	9.60	37.60	-	-	6.60	6.40	8.30	-	2.5-0	5.50
Titanite	-	-	1.40	-	3.40	-	-	-	-	9.91	5.01	3.20

Where Serp: Serpentinite, Epd: Epidosite, Gb: Gabbro, Al. Bs: Altered basalt, Sh. Bs: Sheeted basalt, and P. Bs: Pillow basalt.

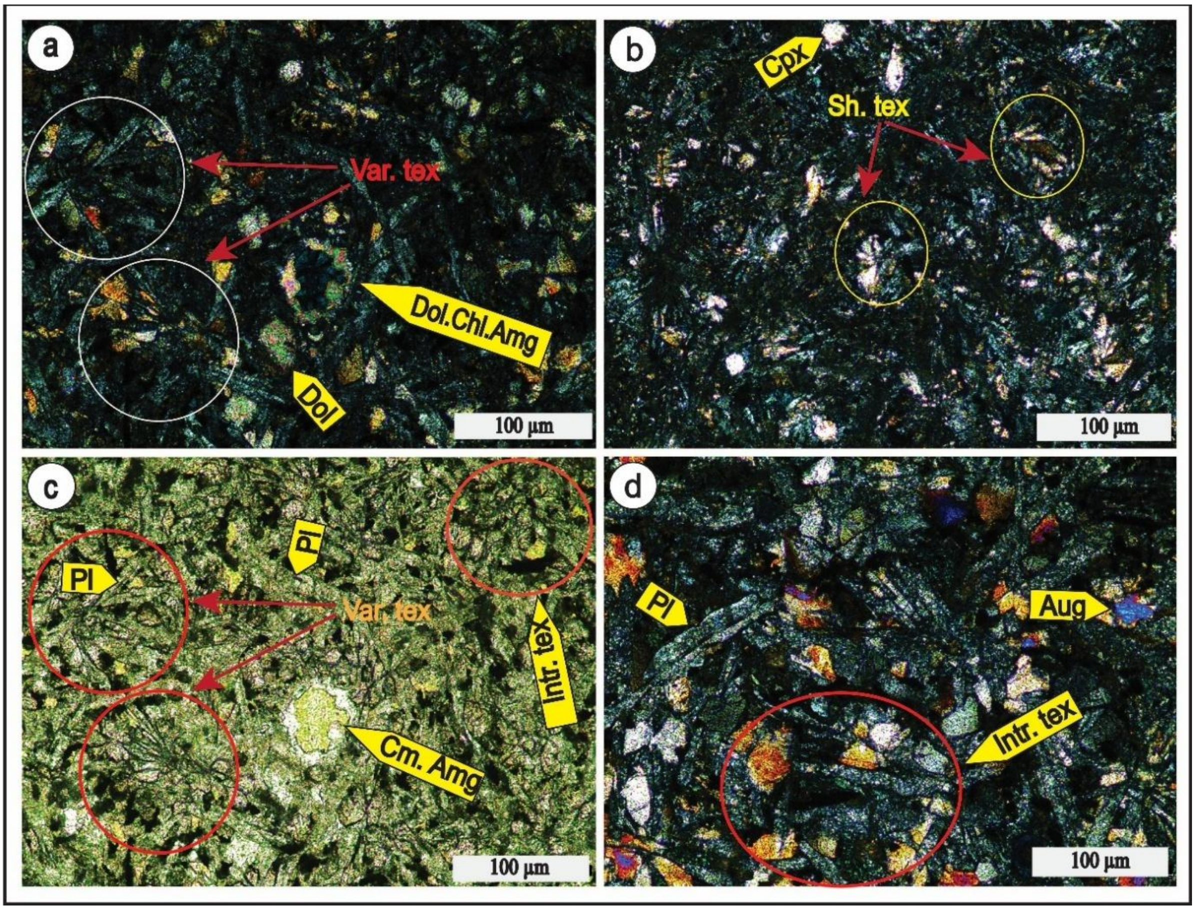

Figure 7. Photomicrograph of pillows exhibit the variation in textural and crystal morphology in three parts of pillow a) variolitic texture and composite amygdules indicate the predominant magmatic and hydrothermal processes b) rim of pillow with abundant sheaf-like textures and microcrystalline minerals c) middle part dominated by variolitic and amygdaloidal textures and d) the core of pillow with holocrystalline and common intergranular texture (where Aug: augite, Cpx: clinopyroxene, Dol: Dolomite, Var.tex: variolitic texture, Sh.tex: sheaf-like texture, Intr.tex: intergranular texture, Dol.Chl.Amg: dolomite, chlorite amygdules Cm.Amg: composite amygdala. Note that the scale for all three parts of the pillow is the same.

3.2.2. Epidosite and sheeted basalt

Epidosite veins appear as dykes cutting through the sheeted basalts, likely formed through metasomatic alteration of basalt. These veins are mainly composed of epidote (35.8 %) and quartz (49.8 %), with minor plagioclase (2.6 – 11.7 %) and hematite (0.2 %; Figure 8a).

The sheeted basalts show varying degrees of alteration. In certain sections, remnants of the original texture are preserved, as seen in the epidote and quartz pseudomorphs after pyroxene and lesser plagioclase (Figure 8b). Primary mineral assemblages in these rocks consist largely of plagioclase (albite 8.7 – 30.4 %, andesine 0.3 – 8.3 %, and anorthite 0.9 %) and pyroxenes (augite 9.7 – 24 % and enstatite 8.3 %), while secondary minerals quartz (37.6 %), chlorite (20.7 – 21.0 %), epidote (1.1 – 21.5 %), magnetite (2.3 %) and dolomite (0.7 %) constitute a significant portion of the altered rock Figure (8c). Textures include intergranular, amygdaloidal, variolitic, and brecciated structures, with abundant vein networks of epidote, chlorite, quartz, and carbonate.

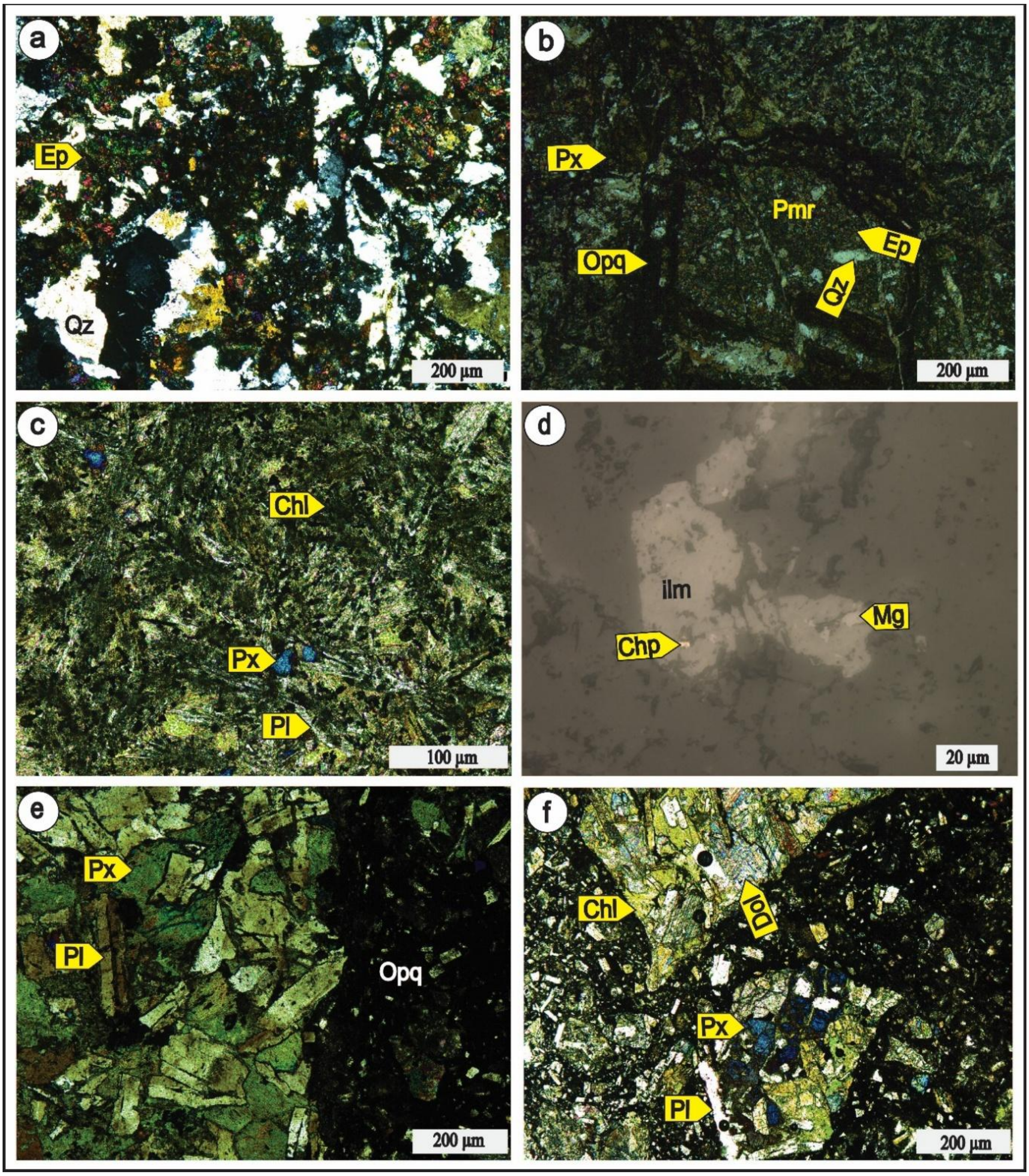

Figure 8. Petrographic images of epidosite and sheeted basalt; a) epidosite dominated by quartz and epidote, formed from the alteration of sheeted basalt, b) altered basalt with relict texture and small proportion of magmatic phases, c) accumulation of major rock-forming d) mineralization of opaque phases in sheeted basalt (reflected light), and e, f) sub-volcanic dyke with brecciation texture bounded by opaque phases (where Opq: opaque phases, Pmr: pseudomorph, Chl: chlorite, Ilm: ilmenite, Mg: magnetite, and Chp: chalcopyrite).

The groundmass consists of cryptocrystalline opaques, pyroxenes, and fine-grained chlorite. The presence of opaque phases such as magnetite, ilmenite, and chalcopyrite in this unit may provide economical potential in the detection of ore-bearing zones (Figure 8d). In addition, these sheeted basalts are intersected by sub-volcanic dykes (Figure 8e), which in some places are brecciated, containing fragments of varied mineral assemblages, ranging from microscopic to macroscopic, within a matrix of opaque minerals and plagioclase laths (Figure 8f).

3.2.3. Gabbro

The gabbroic rocks (Figure 9) are predominantly composed of pyroxenes (enstatite 13.7 %) and plagioclase (albite 41.2 %, andesine 13.2 %, and anorthite 2.3 %), along with minor primary quartz (9.6%), both primary and secondary amphiboles (11.8 %), epidote (6.4 %), titanite (1.4 %) and opaque minerals (Figure 9a, & b). Opaque phases are frequently observed as inclusions within pyroxenes and amphiboles (Figure 9a). Alteration processes such as albitization, uralitization, and epidotization are widespread. Pyroxenes are commonly replaced either partially or completely by amphibole, epidote, and serpentine, while plagioclase alteration largely results in the formation of albite (Figure 9c). The common textures of gabbros are subophitic, intergranular, and myrmekite-like textures (Figure 9d).

3.2.4. Serpentinite

The ultramafic rocks have been completely transformed into serpentinite, with their primary textures fully obliterated. This serpentinite comprises the three major serpentine group minerals, antigorite (63.2 %), chrysotile (29.2 %), and lizardite (4.0 %), accompanied by minor amounts of chromite (2.1 %) and magnetite (1.6 %) These rocks display typical metamorphic fibrous and mesh-like textures, with notable chrysotile and tremolite veinlets reflecting both brittle and ductile deformation Figure (9e, & f).

3.3. Mineral Chemistry

The chemical analyses of plagioclase, clinopyroxene, and titanite are presented in Tables 2, 3, and 4. The samples Hgd.12 and Hgd.15 are selected as representatives for the pillow basaltic rocks of the study area. 22 points were analysed for plagioclase, pyroxene, and titanite as described below.

3.3.1. Plagioclase

Plagioclase is the most common phase in the basaltic rocks, composed mainly of SiO_2, Al_2O_3, Na_2O, and CaO, ranging between (51.82 – 67.1 wt.%), (20.69 – 26.32 wt.%), (5.51 – 10.24 wt.%), and (1.15 – 9.93 wt.%) respectively with small quantity of K_2O (0.37 wt.%) and FeO (1.7 wt.%) on average Table (2). This phase also shows enrichment in Sr and Y and depletion in La. Overall, albite (Ab) occurs in high content, ranging between (50.083% – 93.62% wt.%), with the plots mostly in andesine, albite, and oligoclase fields (Figure 10a). Anorthite (An) varies, ranging from (4.76% to 49.85% wt.%). Such a variation in the value of An in plagioclase is attributed to the exposure of pillows to various degrees of alteration. Orthoclase (Or) makes up the low content (<5.5%) of the plagioclase solid solution.

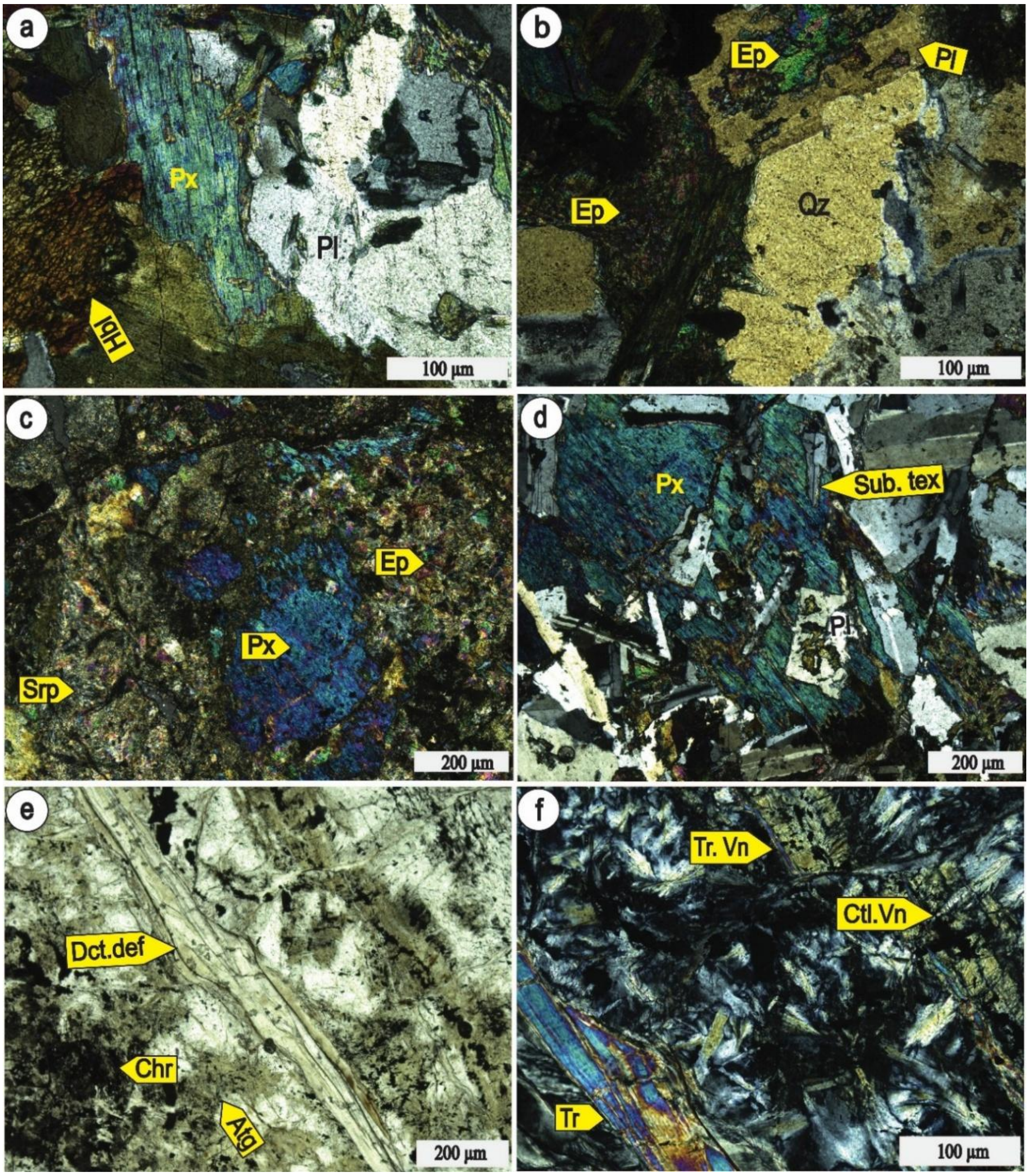

Figure 9. Microscopic images of gabbro and serpentinte exhibit primary and secondary textures and minerals; a) primary amphibole with simple twining positioned on the left part of the view b) primary quartz and plagioclase with epidote inclusion, the uncommon phase of quartz more likely due to oversaturated of melt with silica c) a large pyroxene crystal epidotized from margin with retained its inner part, d) subophitic texture includes a few skeletal plagioclase crystals, and e, f) curved and ruptured chrysotile reflect the evidence of ductile and brittle deformation in serpentinite (where Pl: plagioclase, Px: pyroxene, Hbl: hornblende, Qz: quartz, Ep: epidote, Srp: serpentine, Ep. Vn: epidote vein, Sec. pl: secondary plagioclase, Myr. Tex: myrmecitic-like texture, Sub. Tex: subophitic texture, Atg: antigorite, Chr: chromite, Tr: tremolite, Dct. Def: ductile deformation, Tr. Vn: tremolite vein and Ctl. Vn: chrysotile vein.

3.3.2. Ti-bearing pyroxene

The analysis of major oxides and the calculated numbers of ions obtained from clinopyroxenes of HPB are presented in Table 3. The pyroxenes are the second most abundant minerals after plagioclase and consist largely of SiO_2, CaO, MgO, and FeO, ranging from (45.98 – 48.74 wt.%), (18.55 – 21.72 wt.%), (8.85 – 12.57 wt.%), and (8.58 – 13.81 wt.%) respectively, and small percentage of Al_2O_3 and Na_2O (4.16 – 6.47 and 0.45 – 1.53 wt.%). This phase also contains a significant percentage of TiO_2 in the range between (1.35 – 3.18 wt.%) that could be classified as titaniferous pyroxene. The plotting of pyroxene data on the quadrilateral classification diagram (En- Fs- Di- Hd; Figure 10b) shows that all the selective points, as representative for pyroxenes, fall in the field of augite with a composition of Wo41-43, En27-35, and Fs18-31 in the three end members.

Table 2. Scanning Electronic Microscope (SEM) result showing the oxide content and relative proportions of plagioclase end-member components in representative points of plagioclase for pillow basaltic rocks.

Samples	Hgd.12-01	Hgd.12-02	Hgd.12-03	Hgd.15-01	Hgd.15-02	Hgd.15-03	Hgd.15-04	Hgd.15-05
SiO_2	67.10	67.31	65.51	57.43	57.28	56.50	56.63	51.83
MgO	0.20	0.27	0.26	1.07	0.42	0.39	0.43	1.26
FeO^*	0.50	0.12	0.55	2.79	1.10	0.99	0.77	7.69
Al_2O_3	20.72	20.69	20.74	23.63	25.62	26.33	26.56	21.86
TiO_2	0.00	0.03	0.05	0.04	0.05	0.09	0.08	2.65
Cr_2O_3	0.00	0.02	0.03	0.01	0.03	0.01	0.01	0.25
MnO	0.00	0.04	0.00	0.00	0.01	0.02	0.01	0.01
P_2O_5	0.02	0.06	0.00	0.01	0.01	0.01	0.04	0.01
CaO	1.16	0.94	2.55	6.50	8.56	9.49	9.94	8.56
Na_2O	10.14	10.24	9.99	7.54	6.06	5.78	5.52	5.88
K_2O	0.16	0.27	0.32	0.99	0.85	0.39	0.01	0.00
Sum	100.00	100.00	100.00	100.00	100.00	100.00	100.00	100.00
Si	11.74	11.76	11.55	10.42	10.33	10.19	10.18	9.64
Mg	0.05	0.07	0.07	0.29	0.11	0.10	0.12	0.35
Fe	0.07	0.02	0.07	0.38	0.15	0.13	0.10	1.08
Al	4.27	4.26	4.31	5.06	5.45	5.60	5.63	4.79
Ti	0.00	0.00	0.01	0.01	0.01	0.01	0.01	0.37
Cr	0.00	0.00	0.00	0.00	0.00	0.00	0.00	0.04
Mn	0.00	0.01	0.00	0.00	0.00	0.00	0.00	0.00
P	0.00	0.01	0.00	0.00	0.00	0.00	0.01	0.00
Ca	0.22	0.18	0.48	1.26	1.65	1.83	1.91	1.71
Na	3.44	3.47	3.42	2.65	2.12	2.02	1.92	2.12
K	0.04	0.06	0.07	0.23	0.20	0.09	0.00	0.00
An	5.87	4.76	12.13	30.50	41.69	46.47	49.86	44.58
Ab	93.14	93.62	86.06	63.99	53.39	51.26	50.08	55.42
Or	0.99	1.62	1.81	5.52	4.92	2.28	0.06	0.00

Note: the number of ions calculated based on 32 oxygen, oxides expressed as wt.%, and elements represent the number of cations.

Table 3. SEM representative data of titaniferous pyroxenes showing the oxide wt.% and relative proportion of pyroxene endmember compositions from pillow basalts of Halgurd complex ophiolite.

Samples	Hgd.12-04	Hgd.12-05	Hgd.12-06	Hgd.12-07	Hgd.12-08	Hgd.15-06	Hgd.15-07	Hgd.15-08
SiO_2	48.74	46.03	47.80	45.98	46.61	47.00	48.33	48.36
MgO	11.87	11.97	8.86	11.93	10.48	12.57	13.73	10.52
FeO^*	11.00	10.80	13.48	10.69	13.82	10.91	8.48	12.55
Al_2O_3	4.62	5.80	5.94	6.48	5.86	5.02	4.93	4.16
TiO_2	1.35	2.60	3.18	2.43	1.86	2.27	1.92	2.61
Cr_2O_3	0.02	0.12	0.05	0.22	0.03	0.01	0.01	0.10
MnO	0.20	0.25	0.27	0.19	0.24	0.20	0.05	0.09
P_2O_5	0.07	0.01	0.15	0.17	0.06	0.06	0.06	0.10
CaO	20.66	21.54	18.56	21.02	20.19	21.16	21.72	20.58
Na_2O	1.23	0.66	1.54	0.74	0.65	0.63	0.45	0.83
K_2O	0.23	0.21	0.17	0.14	0.20	0.16	0.31	0.09
Sum	100.00	100.00	100.00	100.00	100.00	100.00	100.00	100.00
Si	1.81	1.72	1.78	1.71	1.74	1.75	1.79	1.80
Mg	0.66	0.67	0.49	0.66	0.58	0.70	0.76	0.58
Fe	0.46	0.46	0.57	0.45	0.58	0.46	0.35	0.53
Al	0.20	0.26	0.26	0.28	0.26	0.22	0.21	0.18
Ti	0.04	0.07	0.09	0.07	0.05	0.06	0.05	0.07
Cr	0.00	0.00	0.00	0.01	0.00	0.00	0.00	0.00
Mn	0.01	0.01	0.01	0.01	0.01	0.01	0.00	0.00
P	0.00	0.00	0.00	0.01	0.00	0.00	0.00	0.00
Ca	0.82	0.86	0.74	0.84	0.81	0.84	0.86	0.82
Na	0.09	0.05	0.11	0.05	0.05	0.05	0.03	0.06
K	0.01	0.01	0.01	0.01	0.01	0.01	0.01	0.00
En	33.88	33.60	27.34	33.96	29.56	34.88	38.40	30.23
Fs	23.76	22.95	31.50	23.04	29.51	22.92	17.96	27.29
Wo	42.36	43.45	41.16	42.99	40.93	42.19	43.65	42.48

Note: the number of oxygen is equal to 6, oxides expressed as wt.%, and elements represent the number of cations.

Table 4. Result of SEM analysis for the selected points of titanite from HPB.

Samples	Hgd.12-09	Hgd.15-09	Hgd.15-10	Hgd.15-11	Hgd.15-12	Hgd.15-13
SiO_2	31.37	31.72	28.19	35.71	37.50	30.36
MgO	0.01	1.65	0.21	0.65	6.52	5.67
FeO^*	2.95	8.70	3.55	4.03	7.61	12.42
Al_2O_3	6.10	4.51	3.16	6.94	3.79	7.66
TiO_2	28.76	28.89	34.10	22.52	19.68	20.26
Cr_2O_3	0.01	0.01	0.01	0.01	0.19	0.01
MnO	0.01	0.01	0.03	0.01	0.02	0.01
P_2O_5	0.01	0.02	0.01	4.82	0.85	1.79
CaO	30.62	24.07	30.33	24.48	22.95	21.30
Na_2O	0.01	0.01	0.01	0.80	0.88	0.28
K_2O	0.14	0.41	0.40	0.04	0.01	0.23
Sum	100.00	100.00	100.00	100.00	100.00	100.00
Si	4.10	4.14	3.75	4.45	4.77	3.94
Mg	0.00	0.32	0.04	0.12	1.24	1.10
Fe	0.29	0.85	0.36	0.38	0.73	1.21
Al	0.94	0.69	0.50	1.02	0.57	1.17
Ti	2.83	2.84	3.41	2.11	1.88	1.98
Cr	0.00	0.00	0.00	0.00	0.02	0.00
Mn	0.00	0.00	0.00	0.00	0.00	0.00
P	0.00	0.00	0.00	0.51	0.09	0.20
Ca	4.29	3.37	4.32	3.27	3.13	2.96
Na	0.00	0.00	0.00	0.19	0.22	0.07
K	0.02	0.07	0.07	0.01	0.00	0.04

Note: the number of ions calculated based on 20 oxygen, oxides expressed as wt.%, and elements represent the number of cations.

3.3.3. Titanite

Titanite occurs as a common accessory phase in the form of cryptocrystalline constituting a substantial portion of intergranular materials, composed mainly of SiO_2, TiO_2, and CaO, vary between (28.19 – 37.50 wt.%), (19.68 – 34.1 wt.%), and (21.3 – 30.62 wt.%) respectively, followed by medium portion of FeO (2.95 – 12.42 wt.%) and Al_2O_3 (3.16 – 7.66 wt.%), and negligible amount of MgO, Cr_2O_3, MnO, P_2O_5, Na_2O and K_2O (< 2 %) (Table 4). In addition, the phase rich in cerium (Ce) and zirconium (Zr), ranges between (0.21 – 0.61 wt.%) and (0.1 – 0.288 wt.%) respectively, while depleted in La, V, and Eu.

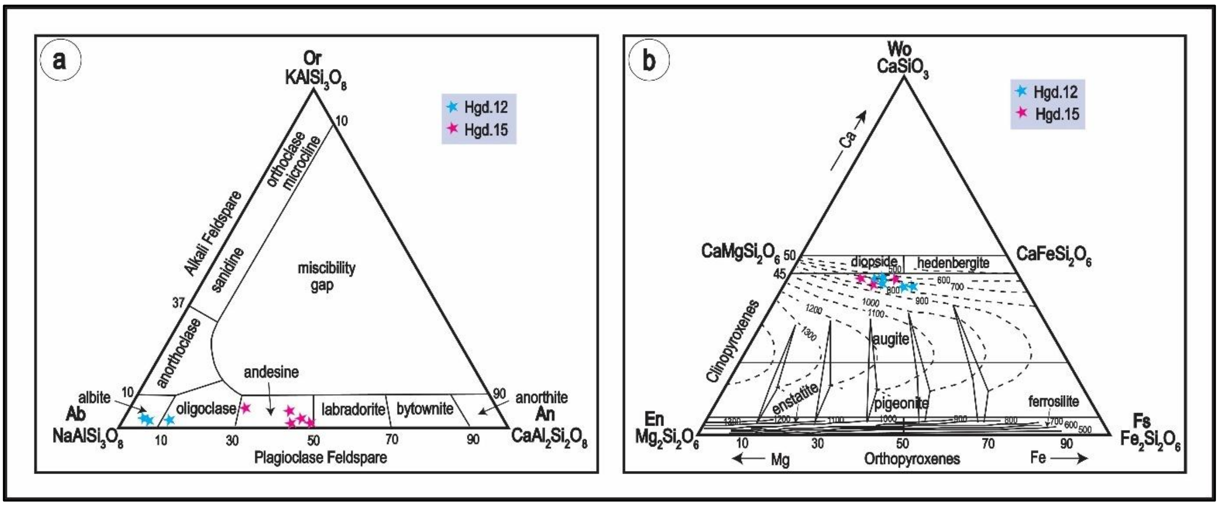

Figure 10. Ternary diagrams illustrating the classification of plagioclase feldspar and pyroxenes, a) (Ab-An-Or) ternary classification diagram adapted from Deer et al. (2013) showing the compositional fields of plagioclase feldspars for HPB, with nearly all the plagioclase representative points falling in the andesine and albite compositional field b) pyroxene classification diagram after Morimoto (1988) based on En-Fs-Wo endmembers and graphical thermometry of pyroxene after Lindsley (1983). All the selected points fall within the augite field with an equilibrium temperature ranging between (600 – 800 °C).

3.4. Geochemistry

The results of the geochemical data are presented in Tables 5 and 6 for both major oxides and trace elements and rare earth elements of pillow basalt, sheeted basalts, gabbro, epidosite, and serpentinite. The dataset includes 20 rock samples. Among them, 11 samples were analysed for pillow basalts and 5 samples for sheeted basalts; the other four samples were taken for supportive information. Chemical analysis of fresh and less altered rock samples shows that the Halgurd basaltic rocks, including both pillows and sheets, are rich in Fe_2O_3, CaO, and TiO_2, varying from (7.73 – 13.3 Wt.%), (6.9 – 11.93 Wt.%), and (1.16 – 2.1 Wt.%) respectively, but low in K_2O (0.1 – 1.92 Wt.%). SiO_2 content in the nominated samples ranges between (47.13 – 51.38 Wt.%), except two sheeted samples (Hgd5 and Hgd17) whose values are 54.80 and 55.51 Wt.%, more likely attributed to alteration processes. Al_2O_3 content in both pillow and sheets ranges between (12.17 – 16.11 Wt.%). TiO_2 proportion is intermediate and has uniform composition in pillow and sheeted samples in the range between (1.15 – 2.1 Wt.%). Loss on ignition (LOI) value for basaltic rocks slightly shows variation in composition that ranges between (1.48 – 3.93 Wt.%) and (3.02 – 5.40 Wt.%) for sheeted and pillow samples, respectively. LOI in serpentinite is high (12.75 Wt. %) due to the role of hydrous minerals. Based on Le Bas (1986) diagram, plotting the geochemical data shows the heterogeneous composition for sheeted basalts, and the samples fall in the basalt, trachybasalt, basaltic andesite, and basaltic trachyandesite fields, while showing the homogeneous composition for pillow basalts that most of the samples plot in the field of basalts and a few in the trachybasalt field (Figure 11a). Such variation in the SiO_2 and alkali element value for sheeted basaltic rocks is attributed to alteration processes rather than pillow basaltic rocks. Furthermore, to achieve a more accurate classification of Halgurd mafic volcanic rocks Zr/TiO_2 vs Nb/Y diagram from Winchester & Floyd (1977) has been used for both pillow and sheeted basalts, in which all the samples plot in the basalt field (Figure 11b).

Table 5. Chemical composition of HPB and the associated rocks shows the oxide weight % and trace element and rare earth elements ppm proportion, from samples (Hgd.1 - Hgd.10).

Samples	**Hgd.1**	**Hgd.2**	**Hgd.3**	**Hgd.4**	**Hgd.5**	**Hgd.6**	**Hgd.7**	**Hgd.8**	**Hgd.9**	**Hgd.10**
Rock Type	**Serp**	**Gb**	**Epd**	**Gb**	**Sh.Bs**	**Sh.Bs**	**P.Bs**	**P.Bs**	**P.Bs**	**P.Bs**
SiO_2(Wt.%)	39.91	47.48	68.31	58.31	55.51	48.49	47.37	47.16	48.87	47.99
Al_2O_3(Wt.%)	1.40	15.04	12.17	14.48	12.59	16.11	15.14	15.84	14.83	15.94
CaO (Wt.%)	0.07	12.22	8.36	5.06	9.82	7.77	8.31	8.81	8.80	7.24
Fe_2O_3(Wt.%)	7.33	13.27	6.93	9.85	9.84	10.23	11.83	11.41	10.98	10.26
K_2O (Wt.%)	0.05	0.05	0.08	0.05	0.05	1.24	0.96	1.11	0.17	1.92
MgO (Wt.%)	37.81	5.23	0.21	2.00	5.12	6.78	6.53	7.74	6.20	7.88
MnO (Wt.%)	0.09	0.24	0.11	0.17	0.15	0.21	0.18	0.19	0.21	0.17
Na_2O(Wt.%)	0.05	2.88	1.76	6.59	1.43	3.97	3.74	2.51	4.73	2.77
P_2O_5 (Wt.%)	0.05	0.10	0.08	0.38	0.19	0.15	0.21	0.18	0.22	0.23
TiO_2 (Wt.%)	0.05	1.44	0.39	1.40	1.31	1.35	1.44	1.62	1.51	1.34
SO_3 (Wt.%)	0.07	0.05	0.10	0.12	0.06	0.07	0.05	0.07	0.13	0.11
BaO (Wt.%)	0.05	0.05	0.05	0.05	0.05	0.05	0.05	0.05	0.05	0.05
LOI (Wt.%)	12.75	2.05	1.48	1.64	3.93	3.62	4.08	3.37	3.35	4.16
Total	99.68	100.10	100.03	100.10	100.05	100.04	99.89	100.05	100.05	100.06
Ba (ppm)	32.00	32.00	39.00	35.00	34.00	140.00	134.00	173.00	65.00	184.00
Ce (ppm)	7.00	7.00	44.00	39.00	14.00	21.00	21.00	26.00	17.00	17.00
Co (ppm)	81.30	37.50	7.30	18.70	29.20	39.70	36.40	44.40	39.20	38.50
Cr (ppm)	2300.00	95.00	184.00	96.00	303.00	281.00	1075.00	284.00	256.00	272.00
Dy (ppm)	0.50	5.90	15.50	12.30	5.30	5.10	5.30	5.90	5.50	4.60
Er (ppm)	0.10	3.50	10.00	7.60	3.20	3.20	3.10	3.50	3.30	2.70
Eu (ppm)	0.10	1.48	2.54	2.52	1.23	1.33	1.38	1.43	1.29	1.18
Gd (ppm)	0.28	3.98	11.45	9.74	4.10	4.16	4.25	4.54	4.46	3.72
Hf (ppm)	0.50	1.20	1.70	1.40	2.30	2.50	2.40	2.50	2.60	2.30
La (ppm)	1.00	5.00	18.00	17.00	9.00	12.00	13.00	13.00	14.00	13.00
Lu (ppm)	0.10	0.50	1.40	1.10	0.50	0.50	0.50	0.50	0.50	0.50
Nb (ppm)	1.00	3.10	10.70	6.70	4.30	9.00	11.10	9.30	8.10	9.80
Nd (ppm)	1.10	9.70	31.90	27.00	11.80	14.30	14.80	15.00	14.60	13.00
Ni (ppm)	2024.00	39.00	5.00	5.00	52.00	94.00	95.00	96.00	84.00	93.00
P (ppm)	87.00	394.00	436.00	1771.00	811.00	877.00	939.00	941.00	902.00	961.00
Pb (ppm)	4.00	4.00	2.00	3.00	1.00	4.00	5.00	4.00	2.00	8.00
Pr (ppm)	0.30	1.86	6.39	5.41	2.45	3.22	3.13	3.13	3.26	2.87
Sm (ppm)	0.20	3.10	9.30	7.90	3.60	3.40	3.70	4.10	3.60	3.20
Sr (ppm)	3.60	366.30	290.50	133.70	283.70	158.40	134.10	131.70	157.50	101.90
Ta (ppm)	0.10	0.40	0.90	0.60	0.40	0.80	0.90	0.80	0.70	1.00
Tb (ppm)	0.10	0.80	2.30	1.90	0.80	0.80	0.90	0.90	0.90	0.80
Th (ppm)	1.10	1.20	1.70	1.40	1.30	2.10	1.90	1.80	1.80	1.90
Ti (ppm)	10.00	8556.00	2612.00	10032.00	8994.00	9693.00	10423.00	12170.00	11051.00	9886.00
Tm (ppm)	0.10	0.50	1.40	1.10	0.50	0.50	0.50	0.50	0.60	0.50
U (ppm)	0.10	0.10	0.20	0.10	0.20	0.30	0.20	0.40	0.30	0.20
V (ppm)	42.00	269.00	16.00	67.00	247.00	261.00	283.00	319.00	291.00	267.00
Y (ppm)	2.00	28.40	81.80	63.20	26.40	25.30	27.80	29.10	28.90	23.50
Yb (ppm)	0.12	3.58	9.64	7.53	3.26	3.23	3.35	3.37	3.31	2.65
Zn (ppm)	50.00	54.00	8.00	29.00	65.00	81.00	88.00	94.00	86.00	80.00
Zr (ppm)	5.00	25.00	51.00	46.00	91.00	102.00	100.00	98.00	99.00	95.00
La/Nb	1.00	1.62	1.68	2.53	2.09	1.33	1.17	1.39	1.72	1.32
Zr/Nb	5.00	8.10	4.80	6.90	21.20	11.30	9.00	10.50	12.20	9.70
Th/Nb	1.10	0.39	0.16	0.21	0.30	0.23	0.17	0.19	0.22	0.19
Nb/Y	0.50	0.11	0.13	0.11	0.16	0.35	0.39	0.31	0.28	0.41
La/Y	0.50	0.17	0.22	0.26	0.34	0.47	0.46	0.44	0.48	0.55
La/Sm	0.50	1.61	1.93	2.15	2.50	3.52	3.51	3.17	3.90	4.06
Sm/Yb	1.67	0.86	0.96	1.05	1.10	1.05	1.10	1.21	1.08	1.20
La/Nb	1.00	1.61	1.68	2.53	2.09	1.34	1.17	1.39	1.72	1.32
Nb/U	10.00	31.00	53.50	67.00	21.50	30.00	55.50	23.25	27.00	49.00
Nb/Zr	0.20	0.12	0.21	0.14	0.047	0.08	0.11	0.09	0.08	0.10
Ti/V	0.23	31.80	163.25	149.70	36.41	37.13	36.83	38.15	37.97	37.02
Nb/Yb	8.34	0.86	1.11	0.89	1.32	2.78	3.31	2.75	2.44	3.69
Y/Nb	2.00	9.16	7.64	9.43	6.13	2.81	2.50	3.12	3.57	2.40
Zr/Y	2.50	0.88	0.62	0.73	3.45	4.03	3.60	3.37	3.43	4.04
Th/Yb	9.17	0.34	0.18	0.19	0.40	0.65	0.57	0.53	0.54	0.72

Table 6. Chemical composition of HPB and the associated rocks from samples (Hgd.11 - Hgd.18).

Samples	**Hgd.11**	**Hgd.12**	**Hgd.13**	**Hgd.14C**	**Hgd.14M**	**Hgd.14E**	**Hgd.15**	**Hgd.16**	**Hgd.17**	**Hgd.18**
Rock Type	**P.Bs**	**P.Bs**	**P.Bs**	**P.Bs**	**P.Bs**	**P.Bs**	**P.Bs**	**Sh.Bs**	**Sh.Bs**	**Sh.Bs**
SiO_2(Wt.%)	49.21	48.41	49.32	47.20	49.35	50.03	47.13	49.44	54.8	51.38
Al_2O_3(Wt.%)	14.77	14.27	13.90	14.49	13.76	14.45	14.43	14.33	15.32	13.72
CaO (Wt.%)	11.93	10.82	9.16	8.70	7.02	7.53	8.70	7.95	4.57	6.91
Fe_2O_3(Wt.%)	7.73	9.12	10.21	12.95	12.03	11.51	12.97	12.23	10.33	13.30
K_2O (Wt.%)	0.05	0.24	0.13	0.96	0.29	0.11	0.60	0.27	0.33	0.10
MgO (Wt.%)	6.23	5.06	5.21	6.98	6.47	6.08	7.32	6.51	3.95	3.97
MnO (Wt.%)	0.12	0.15	0.13	0.19	0.16	0.17	0.18	0.17	0.14	0.25
Na_2O(Wt.%)	3.64	5.17	4.92	2.98	3.89	4.77	2.78	3.92	6.03	3.99
P_2O_5 (Wt.%)	0.05	0.19	0.22	0.27	0.23	0.25	0.26	0.27	0.24	0.34
TiO_2 (Wt.%)	0.88	1.16	1.33	2.07	1.94	1.99	2.07	2.02	1.29	2.10
SO_3 (Wt.%)	0.05	0.05	0.12	0.05	0.70	0.10	0.17	0.11	0.09	0.24
BaO (Wt.%)	0.05	0.05	0.05	0.05	1.09	0.05	0.05	0.05	0.05	0.05
LOI (Wt.%)	5.38	5.41	5.38	3.17	3.05	3.02	3.39	2.78	2.90	3.72
Total	100.11	100.10	100.07	100.06	98.94	100.04	100.05	100.05	100.04	100.06
Ba (ppm)	40.00	78.00	57.00	154.00	93.00	63.00	118.00	88.00	72.00	67.00
Ce (ppm)	14.00	26.00	24.00	19.00	22.00	23.00	21.00	22.00	29.00	26.00
Co (ppm)	33.50	28.91	29.00	42.70	44.90	41.10	43.40	53.70	29.20	25.10
Cr (ppm)	343.00	273.00	218.00	208.00	203.00	182.00	191.00	180.00	145.00	86.00
Dy (ppm)	3.30	4.40	4.80	6.70	6.40	6.10	7.20	7.00	7.20	10.30
Er (ppm)	1.90	2.60	2.80	3.70	3.80	4.00	4.10	4.20	4.30	5.80
Eu (ppm)	0.78	1.14	1.20	1.59	1.59	1.49	1.67	1.76	1.76	2.59
Gd (ppm)	2.58	3.70	4.09	5.36	5.29	5.11	5.89	5.60	6.19	8.20
Hf (ppm)	1.60	2.20	2.20	2.50	2.90	2.90	2.70	2.60	3.00	2.90
La (ppm)	8.00	15.00	14.00	11.00	10.00	11.00	12.00	12.00	15.00	11.00
Lu (ppm)	0.30	0.40	0.50	0.60	0.60	0.60	0.60	0.70	0.60	0.80
Nb (ppm)	5.70	10.00	9.50	6.00	7.10	3.40	3.80	1.30	8.50	1.70
Nd (ppm)	8.30	13.90	14.10	15.50	15.80	15.90	17.00	16.50	19.90	21.30
Ni (ppm)	83.00	75.00	53.00	53.00	76.00	53.00	56.00	69.00	28.00	2.00
P (ppm)	539.00	890.00	949.00	1067.00	1095.00	1016.00	1106.00	945.00	1216.00	1458.00
Pb (ppm)	1.00	3.00	2.00	1.00	4.00	2.00	1.00	6.00	6.00	4.00
Pr (ppm)	1.74	3.14	3.10	3.27	3.25	3.15	3.45	3.35	4.22	4.12
Sm (ppm)	2.20	3.40	3.50	4.60	4.60	4.40	4.90	4.80	5.20	6.80
Sr (ppm)	65.10	124.10	70.70	114.50	137.80	131.10	100.20	153.00	122.80	204.70
Ta (ppm)	0.50	0.80	0.90	0.50	0.50	0.30	0.30	0.10	0.50	0.20
Tb (ppm)	0.50	0.70	0.80	1.10	1.10	1.10	1.10	1.10	1.20	1.60
Th (ppm)	1.50	2.10	2.00	1.60	1.60	1.60	1.60	1.60	2.10	1.20
Ti (ppm)	6226.00	8402.00	9849.00	13516.00	14098.00	12059.00	14338.00	9159.00	9437.00	11162.00
Tm (ppm)	0.30	0.40	0.50	0.60	0.60	0.60	0.60	0.60	0.60	0.90
U (ppm)	0.20	0.20	0.40	0.20	0.60	0.30	0.30	0.50	0.30	0.20
V (ppm)	209.00	235.00	254.00	327.00	346.00	309.00	348.00	271.00	171.00	140.00
Y (ppm)	16.30	22.00	23.90	32.40	32.60	31.70	34.60	34.30	38.70	53.70
Yb (ppm)	1.86	2.36	2.88	3.58	3.75	3.76	3.89	4.35	4.07	5.46
Zn (ppm)	52.00	62.00	72.00	101.00	101.00	96.00	100.00	105.00	105.00	116.00
Zr (ppm)	56.00	89.00	92.00	87.00	117.00	124.00	98.00	101.00	115.00	105.00
La/Nb	1.40	1.50	1.47	1.83	1.40	3.23	3.15	9.23	1.76	6.47
Zr/Nb	9.80	8.90	9.70	14.50	16.50	36.50	25.80	77.70	13.50	61.80
Th/Nb	0.26	0.21	0.21	0.27	0.23	0.47	0.42	1.23	0.25	0.71
Nb/Y	0.34	0.45	0.39	0.18	0.21	0.11	0.11	0.03	0.22	0.03
La/Y	0.49	0.68	0.58	0.33	0.30	0.34	0.34	0.34	0.38	0.21
La/Sm	3.63	4.41	4.00	2.39	2.17	2.50	2.44	2.50	2.88	1.61
Sm/Yb	1.18	1.44	1.21	1.28	1.22	1.17	1.26	1.10	1.27	1.24
La/Nb	1.40	1.50	1.47	1.83	1.40	3.23	3.15	9.23	1.76	6.47
Nb/U	28.20	50.00	23.75	30.00	11.83	11.34	12.67	2.60	28.34	8.50
Nb/Zr	0.10	0.11	0.10	0.06	0.06	0.03	0.04	0.01	0.07	0.02
Ti/V	29.78	35.75	38.77	41.34	40.74	39.02	41.20	33.79	55.18	79.72
Nb/Yb	3.06	4.23	3.29	1.67	1.89	0.90	0.97	0.29	2.09	0.31
Y/Nb	2.85	2.20	2.51	5.40	4.59	9.32	9.10	26.38	4.55	31.58
Zr/Y	3.44	4.05	3.85	2.69	3.59	3.91	2.83	2.94	2.97	1.96
Th/Yb	0.81	0.89	0.69	0.45	0.43	0.43	0.41	0.37	0.52	0.22

Note: three samples were taken for Hgd.14 from inner, middle, and outer parts of the pillow, where Serp: serpentinite, Gb: Gabbro, Epd: epidosite, Sh.Bs: sheeted basalt, and P.Bs: pillow basalts.

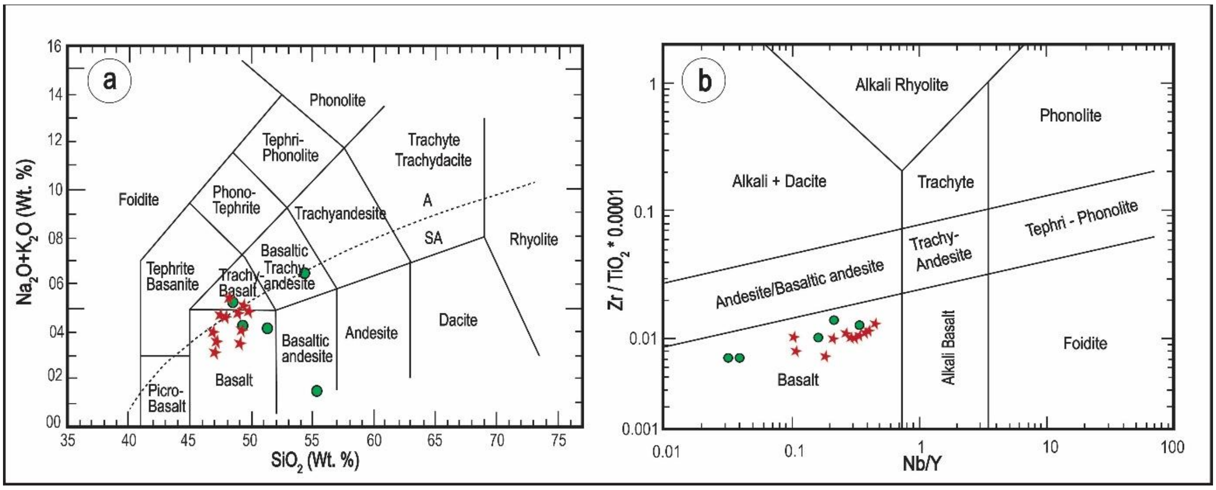

Figure 10. chemical classification diagrams based on oxide and immobile elements showing the Halgurd pillow basaltic rocks, almost all the samples plot in the basalt field, indicating a prevalent mafic composition. a) classical geochemical classification diagram after Le Bas (1986) displays the homogenous composition for pillow basaltic rocks, with the majority of samples falling in the basalt field, but heterogamous composition for sheeted basalt samples, b) Nb/Y vs. Zr/TiO_2 diagram based on *Winchester & Floyd (1977)* showing the samples cluster within the basalt domain, providing accurate classification resistant to alteration processes.

The normalized pillow basaltic samples to the standard primitive mantle (Figure 12a) display a semi-flat, gentle pattern with light rare earth element (LREE) being considerably enriched compared to the heavy rare earth element (HREE), similar to the E-MORB pattern. Among the HREE, yttrium (Y) has the lowest value as it is presented in a negative anomaly on the right side of the spider diagram. However, (Eu/Eu) N values vary between 5 and 10.84, but there are no notable europium (Eu) anomalies. The patterns also show that the ascended mafic lava is depleted in Nb and Ta with clear negative anomalies usually associated with arc-related magma generated in the supra-subduction zone. In addition, the Chondrite-normalized multi-REE patterns for pillows display a significantly enriched character with a lack of Eu anomalies similar to the basaltic samples found in a typical P-MORB setting (Figure 12b).

The spider pattern normalized to the primitive mantle for the sheeted basalts (Figure 12c) depicts a flat pattern similar to that of pillows with a high concentration of light rare earth elements relative to HREE but relatively stronger Nb and Ta anomalies. The pattern is also characterized by a lack of Eu anomaly, ranging from 7.98 to 16.81, a slightly greater ratio than that of pillows. The enrichment of sheets in LREE, as well as the presence of negative Nb and Ta anomalies, makes the patterns have mutual affinity to the P-MORB and arc-related basalt. Negative Ti anomaly in sheeted sample patterns is a distinctive geochemical property that sets them apart from those of pillows that lack it. Plotted spider pattern normalized to standard chondritic Figure (12d) values exhibit that sheeted basaltic lava is clearly enriched in LREE compared to HREE. Additionally, these samples show greater middle rare earth elements (MREE) levels than those of pillows.

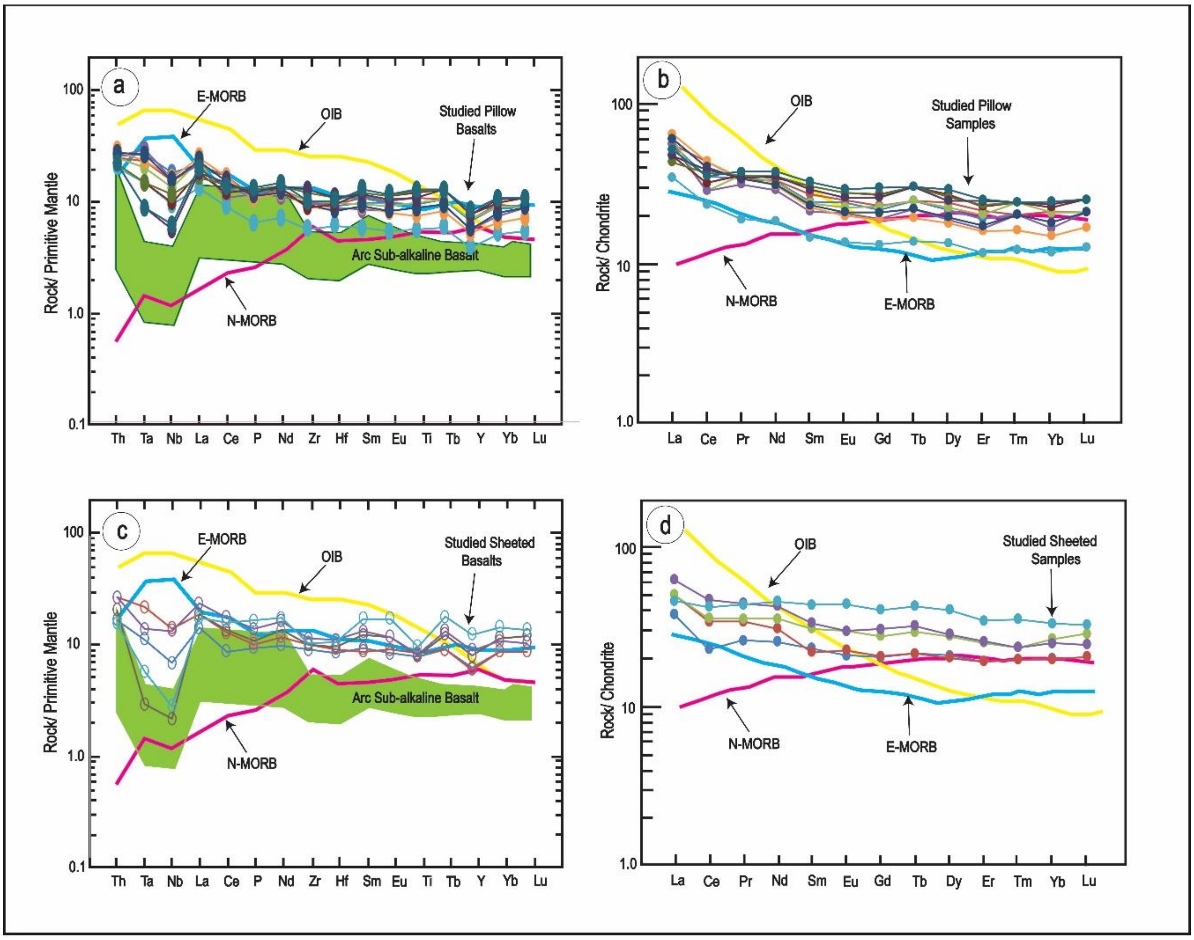

Figure 11. Normalization of Halgurd volcanic rocks to primitive mantle and chondrite. a, b) Normalized Halgurd pillow basaltic rocks to primitive mantle and chondrite, and c, d) multi-element diagrams show the normalization of sheeted basalts to primitive mantle and chondrite *(Sun & McDonough, 1989)*.

4. Discussion

4.1. Magmatic affinity and petrogenesis

The classical AFM diagram has not been applied to the Halgurd volcanic rocks to discriminate the magmatic series since the rocks experienced a great effect of alteration. Instead, immobile element diagrams such as TiO_2 vs. Zr/ P_2O_5 and Nb/Y vs. Zr/P_2O_5 diagrams from *Winchester & Floyd (1977)* were used, and according to these diagrams, the tholeiitic characteristics dominate in the basaltic pillow samples (Figure 13a & b). To trace magmatic evolution and fractionation trends, variation diagrams were used, with Zr on the x-axis due to its low mobility during alteration (Figure 14). In the Zr vs. Y diagram used by *Capan & Floyd (1985;* Figure 14a), both pillow and sheeted samples show a positive correlation. The consistent Zr/Y ratios suggest uniform partial melting of the parent rock. However, samples with low Zr and high Cr show a negative trend in the Zr vs. Cr diagram (Figure 14b)—likely reflecting a higher degree of partial melting. Based on trace element variation diagrams using Zr as a differentiation index that was first discussed by *Capan & Floyd (1985)*, Pillow samples show the great effect of fractional crystallization during the trend of magmatic evolution. Harker-type diagrams (Figure 14) also indicate that the Halgurd mafic volcanic rocks experienced fractional crystallization. The negative SiO_2–MgO trend in pillow samples (Figure 14c) suggests olivine removal. Additionally, the moderate MgO content (5.2 – 7.88 wt.%) reflects significant magma evolution, as primary magmas typically contain at least twice that amount.

Cr and Ni, as stable and compatible elements, closely reflect the composition of the parental melt and serve as more reliable alteration indicators than the Mg# of basalts, which is more affected by alteration and weathering. In unaltered basalts, Cr and Ni typically range from 280 – 550 ppm and 75 – 140 ppm, respectively *(Humphris & Thompson, 1978)*. In the Halgurd pillow basalts, Cr and Ni range from 182 – 343 ppm and 53 – 96 ppm, with one exception—sample Hgd.7, which contains 1075 ppm Cr. Overall, these values are significantly lower than those expected in primitive magmas, indicating depletion through fractional crystallization and removal of olivine, spinel, and clinopyroxene during magma evolution.

Yttrium (Y), an incompatible element, behaves like HREEs and is readily incorporated into amphibole and garnet but less so in pyroxene. Accessory minerals such as apatite and titanite can also significantly affect Y concentrations by accommodating it in their structures (Green, 1980; Lambert et al., 1974). The negative Y anomaly in Halgurd mafic volcanic rocks, normalized to primitive mantle, is likely due to amphibole fractionation or apatite presence rather than garnet or titanite. This is supported by low Ce/Yb ratios indicating no residual garnet (Gaetani et al., 2003; Mckenzie & O'nions, 1991) and high Ti contents in titanite (20 – 28 wt.%) and pyroxene (1.35 – 3.18 wt.%) from SEM analyses, suggesting titanite is absent in the residual parental rock. This points to amphibole-dominated fractionation as a key process influencing magma evolution.

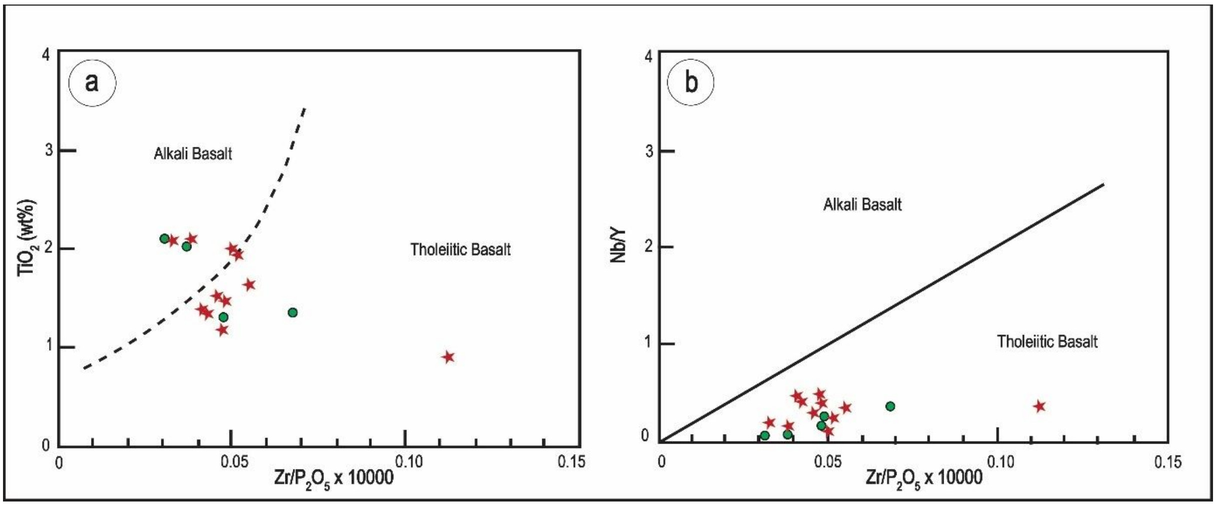

Figure 12. Magmatic characteristics of Halgurd volcanic rocks based on immobile elements, a) TiO_2 vs. Zr/ P_2O_5, and b) Nb/Y vs. Zr/P_2O_5 diagrams applied by *Winchester & Floyd (1977)*, confirm the tholeiitic basalt for Halgurd mafic volcanic rocks. The red circles represent pillow basalts, while the green circles represent the basalt sheets.

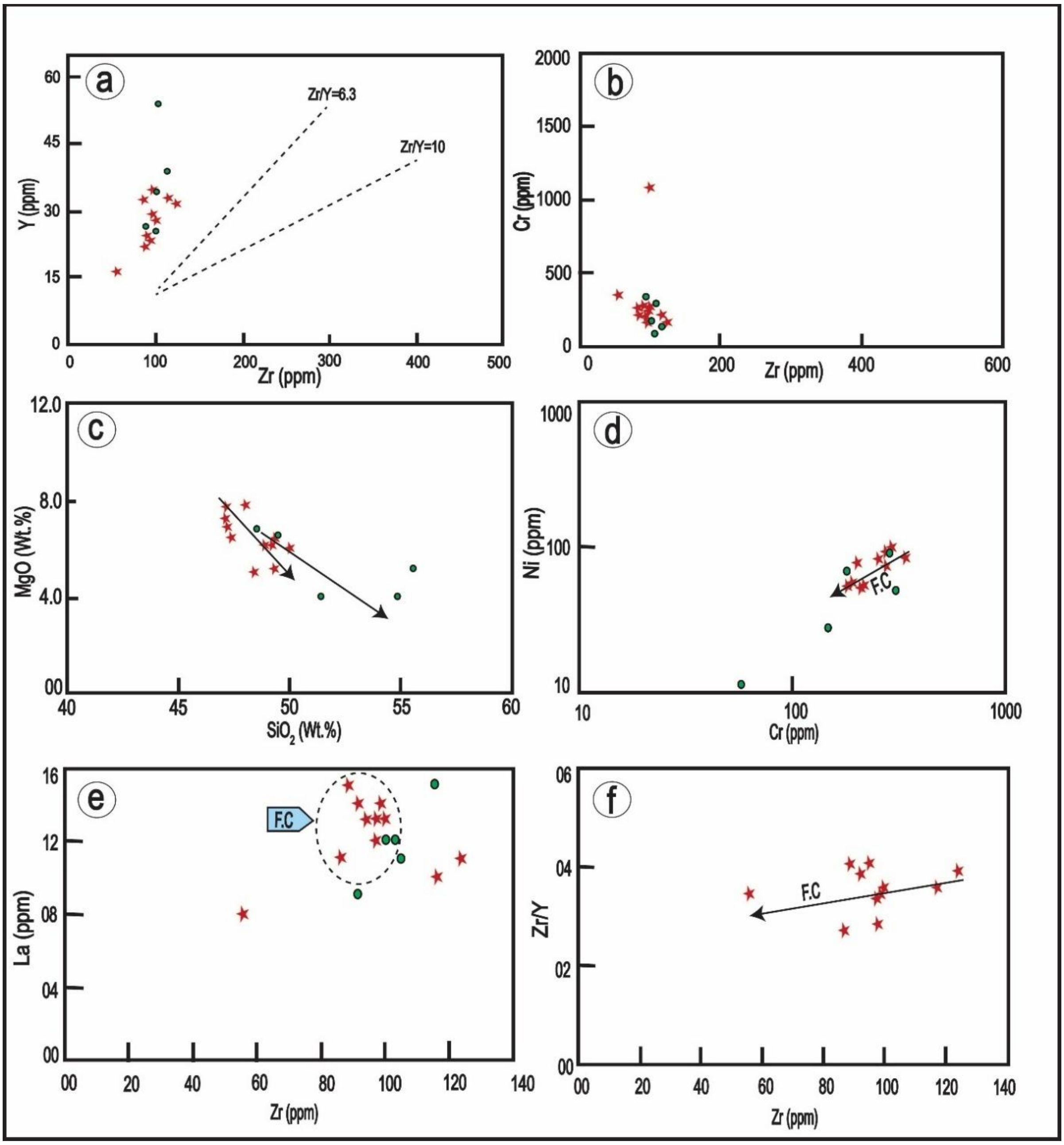

Figure 13. Compatible and incompatible trace elements for Halgurd pillow and sheeted basalts against Zr diagrams after *Capan & Floyd (1985)* a) Zr vs. Y shows the positive linear trend for both pillow and sheeted basalts, indicate the dominant control of fractional crystallization b) Zr vs. Cr displays the negative trend for the samples, supporting the progressive magmatic evolution by fractional crystallization rather than partial melting, and c, d, e, f) display the relationship between magmatophile and hygromagmatophile elements; the arrows refer to the fractional crystallization of magma during the formation of mafic volcanic rocks and segregation of olivine crystals from the rest of the melt.

The Ce/Yb ratio in basaltic rocks helps assess magma source depth. Partial melting of spinel peridotite produces melts with low Ce/Yb ratios, indicating no residual phases retain HREEs. Conversely, high Ce/Yb ratios suggest residual garnet presence, as garnet preferentially retains

Yb over Ce *(Gaetani et al., 2003; Mckenzie & O'nions, 1991)*. Partial melting of garnet-bearing peridotite typically yields Ce/Yb ratios above 20 (Ellam, 1992). In Halgurd mafic volcanic rocks, Ce/Yb ratios range from 4.28 – 7.12 (sheeted) and 5.13 – 11.01 (pillow), supporting a spinel-peridotite source (Figure 15). This indicates magma generation at shallower mantle depths, typical of mid-ocean ridge or back-arc settings.

4.2. Tectonic setting

Multiple tectonomagmatic diagrams using immobile elements were applied to the Halgurd mafic volcanic rocks to infer their paleotectonic setting (Cann, 1970). Key elements include Ti, P, Zr, Y, Nb, Ta, Hf, Th, mid- and heavy REEs, and transition metals like Ni, Co, Cr, and V.

On the Nb/Zr vs. Ba/Zr diagram after Ishizuka et al. (1990) (Figure 16a), pillow basalts plot mainly within the back-arc basin basalt (BABB) field, extending toward enriched mid-ocean ridge basalts (E-MORB). Sheeted samples also cluster in the BABB field but show less affinity to E-MORB. Both groups exhibit low Nb/Zr and Ba/Zr ratios without significant correlation.

In the V vs. Ti/1000 plot, Shervais (1982) Figure (16b), pillow basalts align with MORB and BABB fields, with Ti/V ratios mostly between 20 and 50. Sheeted basalts fall in similar fields except samples Hgd.17 and Hgd.18, which have low V and high Ti. Their high Ti/V ratios (30 – 50) indicate less oxidized mantle conditions than typical supra-subduction arc magmas, which have low Ti/V due to high vanadium from slab dehydration (Chaib et al., 2021).

The Ba/Nb vs. La/Nb diagram *Manikyamba & Kerrich (2011)* Figure (16c) shows elevated La/Nb and Ba/Nb ratios, especially in sheeted samples, indicating an arc volcanic influence, overlapping with MORB fields.

On the Y/Nb vs. Zr/Nb diagram, *L. Xia & Li (2019;* Figure 16d), most samples plot near E-MORB with low Y/Nb and Zr/Nb ratios. Exceptions are two sheeted samples (Hgd.16 and Hgd.18) with high Zr/Nb ratios (77.69 and 61.76), placing them near N-type MORB.

Immobile multi-element diagrams Figure (16) display geochemical signatures transitional between arc-related magmas and mid-ocean ridge basalts (MORB), consistent with a back-arc basin (BAB) setting influenced by subduction-modified mantle sources (Fretzdorff et al., 2002). Negative Nb and Ta anomalies typical of volcanic arcs are present, but Nb/Y vs. Zr/Y Figure (16e) plots also indicate a mantle source influenced by plume components (Condie, 2005). Elevated Th/Yb ratios (Figure 16f) further support a subduction-modified mantle source (Pearce, 2008; RL, 2005). Additionally, vesicle textures dominated by small, sparse vesicles, consistent with formation in relatively deep water, support a back-arc basin origin rather than a typical mid-ocean ridge environment.

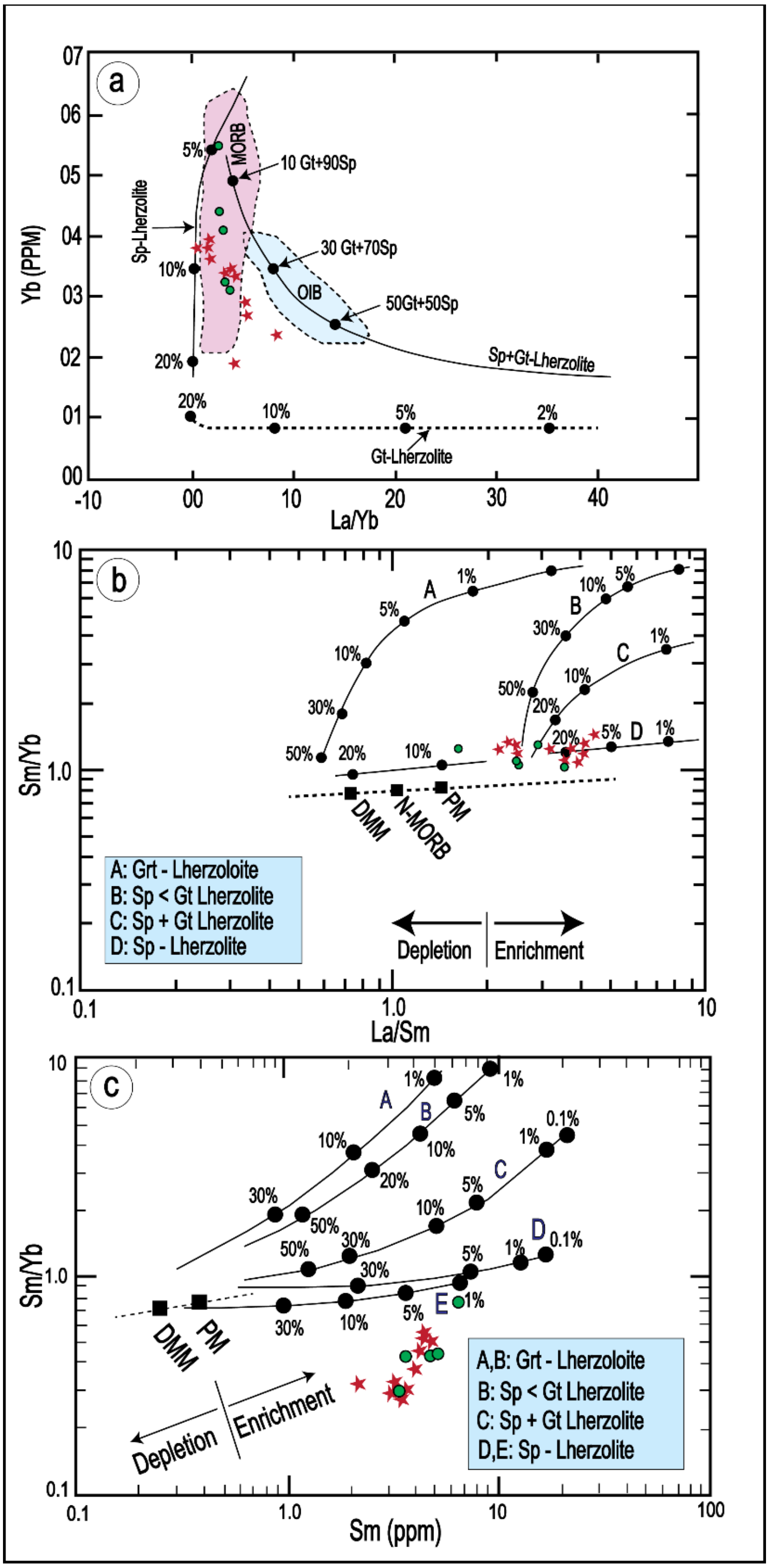

Figure 15. Partial melting diagrams illustrating the melting degree of the parent rocks. Yb vs. La/Yb, Sm/Yb vs. La/Sm, and Sm/Yb vs. Sm diagrams used by Aldanmaz et al. (2000) demonstrate the rate of partial melting for Halgurd pillow and sheeted basaltic rocks. Almost all samples are plotted close to the spinel-Lherzolite source with partial melting ranges between (6%-16%) and (8%-10%) for both pillow and sheeted samples, respectively.

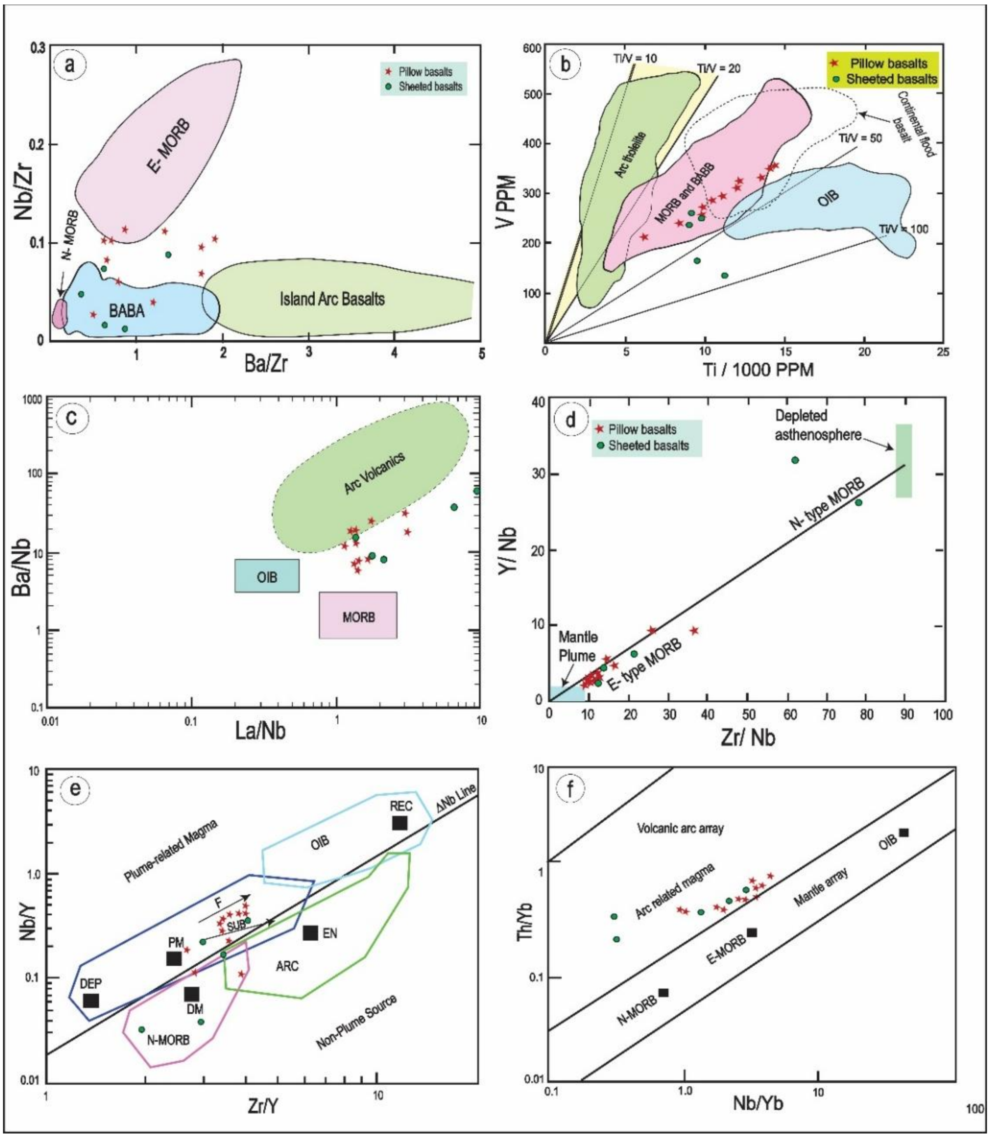

Figure 14. Discrimination diagrams illustrating the tectonomagmatic of Halgurd pillow and sheeted basalts, a) Nb/Zr vs. Ba/Zr. Ishizuka et al. (1990): the samples plot in the field of BABA with affinity to E-MORB type b) V vs. Ti Shervais (1982): the samples show positive trend and fall within the MORB & BABB field c) the high Ba/Nb and La/Nb ratios have made the samples to have MORB and arc volcanic characteristics d) the low Y/Nb and Zr/Nb ratios within Halgurd mafic volcanic rocks suggesting a magma originally associated to Plume influenced mid-oceanic ridge basalt (P-MORB) e) Nb/Y vs. Zr/Y diagram Condie (2005) presenting the studied samples in the field of plume-derived magma without the effect of recycling components. Arrows indicate effects of batch melting (F) and subduction (SUB) and f) Th/Yb vs. Nb/Yb diagram Pearce (2008) displaying the samples plotted out of the mantle array in the vicinity of arc- volcanic rocks and the mantle array where (MORB: mid-oceanic ridge basalt, N-MORB: normal mid-oceanic ridge basalt, E-MORB: enriched mid-oceanic ridge basalt, BABB: back arc basin basalt, MORB & BABB: mid-oceanic ridge basalt and back arc basin basalt, OIB: ocean island basalt, OIB=Oceanic Island Basalt, DM=Shallow Depleted Mantle, DEP=Deep Depleted Mantle, EN= Enriched Component, REC=Recycled Component, and PM: primitive mantle).

However, certain discrimination diagrams, such as Nb/Y vs. Zr/Y diagram Condie (2005) plot the samples into an enriched field that coincides with plume signatures, the regular negative Nb–Ta depletion pattern, and elevated Th/Yb ratios indicate the non-involvement of plume inputs. Instead, they reflect slab-modified enriched MORB in a back-arc basin setting, typically developed from upwelling of E-MORB-like magma that is partially modified by the melt yield from the interaction of slab-derived fluids with the overlying mantle wedge.

Furthermore, the moderate TiO_2 content (1.5 – 2.1 wt.%) and La/Yb_n ratios (1.83 – 4.37) in pillows support the back-arc basin setting for the HPB, approximately similar ranges found in the basalts of the Rudny Altai with TiO_2 content range between (0.96 – 1.92 wt%) and La/Yb_n ratios (0.9 – 2.8) (for more information, see Kuibida, 2019).

4.3. Geodynamic Implication

During the opening of the Neo-Tethys Ocean, two major volcanic arc–rift systems developed along the Iraqi Zagros Suture Zone (IZSZ): the robust Hasanbag and Walash-Naopurdan arc–back-arc extensional regimes. The Cretaceous Hasanbag arc complex formed as part of the Neotethyan oceanic crust subducted during the early Cretaceous (106 – 92 Ma), coinciding with the Oman and Neyriz ophiolites (95 and 93 Ma) and the late Cretaceous obduction of Hasanbag ophiolite onto the Arabian passive margin, synchronous with the emplacement of Kermanshah and Penjween ophiolites (S. A. Ali et al., 2012).

Geographically and Tectonically, the Halgurd back-arc basin is juxtaposed with the Hasanbag arc complex, forming the Hasanbag–Halgurd arc–back-arc magmatic system within the Zagros orogenic belt (Figure 17). Since back-arc spreading initiates after subduction onset, the Halgurd basin is younger than the Hasanbag island arc, consistent with Honz's (1991) observation that back-arc basins form roughly 15 Ma after arc volcanism begins.

The late Cretaceous Hasanbag ophiolite–arc complex is poorly preserved due to later obduction, arc–continent collision, and ongoing Arabia–Eurasia convergence (S. A. Ali, 2012; S. A. Ali et al., 2012). In contrast, the Halgurd ophiolite sequence is well-preserved, comprising serpentinite, gabbro, sheeted basalts, pillow basalts, and cherts. Despite intense deformation, sedimentary chert layers are observed near serpentinite intrusions (Figure 18). Unlike the Bulfat ophiolite, where the sheeted dyke section is absent, the Halgurd complex may represent a complete ophiolite sequence within the Iraqi Zagros orogenic belt.

Subduction initiation and its nature remain a key but debated process in plate tectonics (Hall, 2019; Mackay-Champion et al., 2024; Stern, 2004; Tong et al., 2024). Two end-member models are recognized: spontaneous subduction initiation (SSI) and induced subduction initiation (ISI), distinguished mainly by the role of gravitational instability driving old lithosphere downward *(Stern & Gerya, 2018; Zhou & Wada, 2021).* Time gaps between forearc rocks and associated ophiolites can help differentiate SSI (simultaneous evolution) from ISI (multi-million-year lag) (Guilmette et al., 2023; Van Hinsbergen et al., 2015).

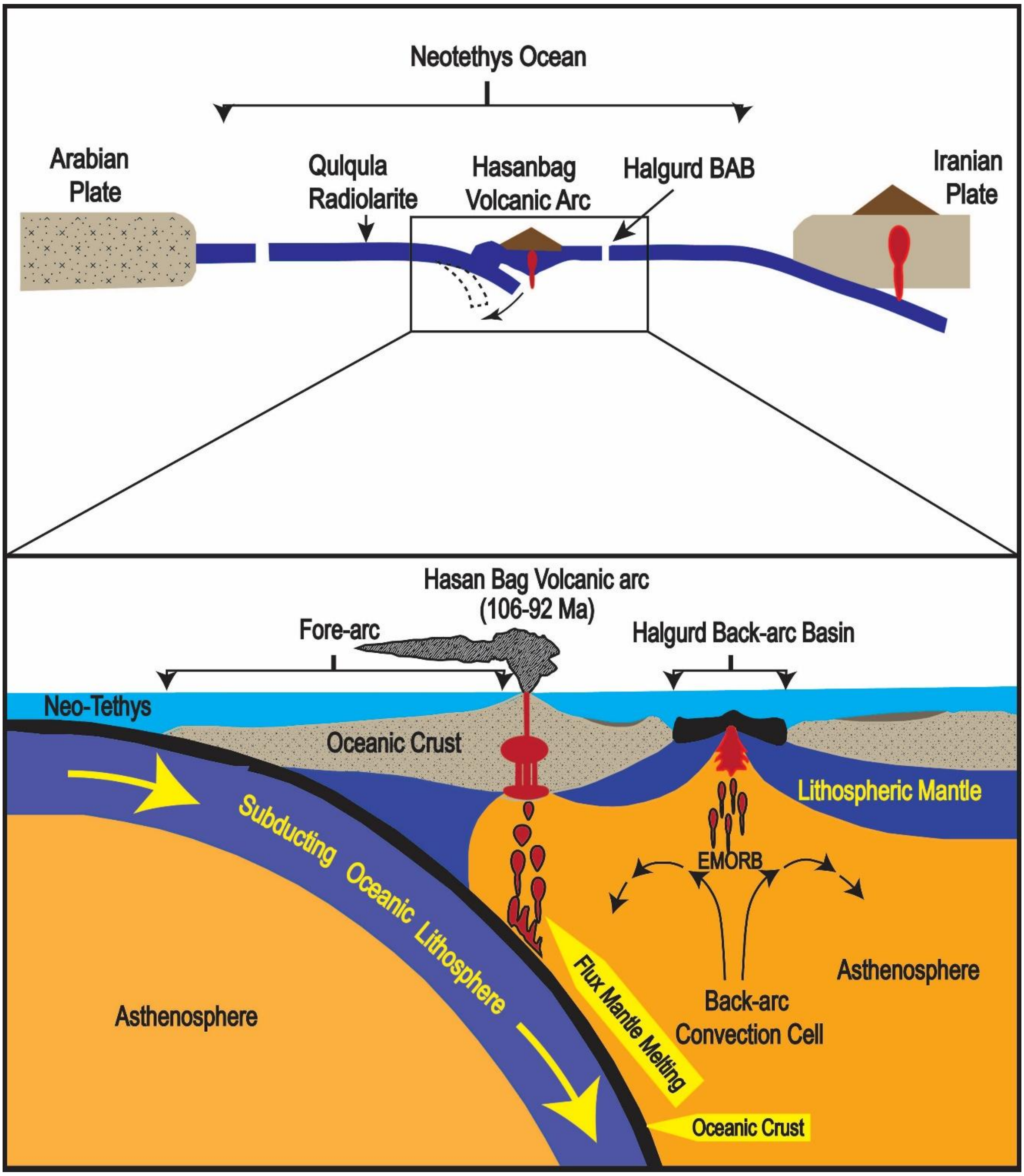

Figure 17. The geodynamic model of the Back arc basin associated with a subduction zone showing the tectonic features of the Hasanbag-Halgurd arc-back arc magmatic system with 106 – 92 Ma for the evolution of the Hasanbag volcanic arc (S. A. Ali et al., 2012).

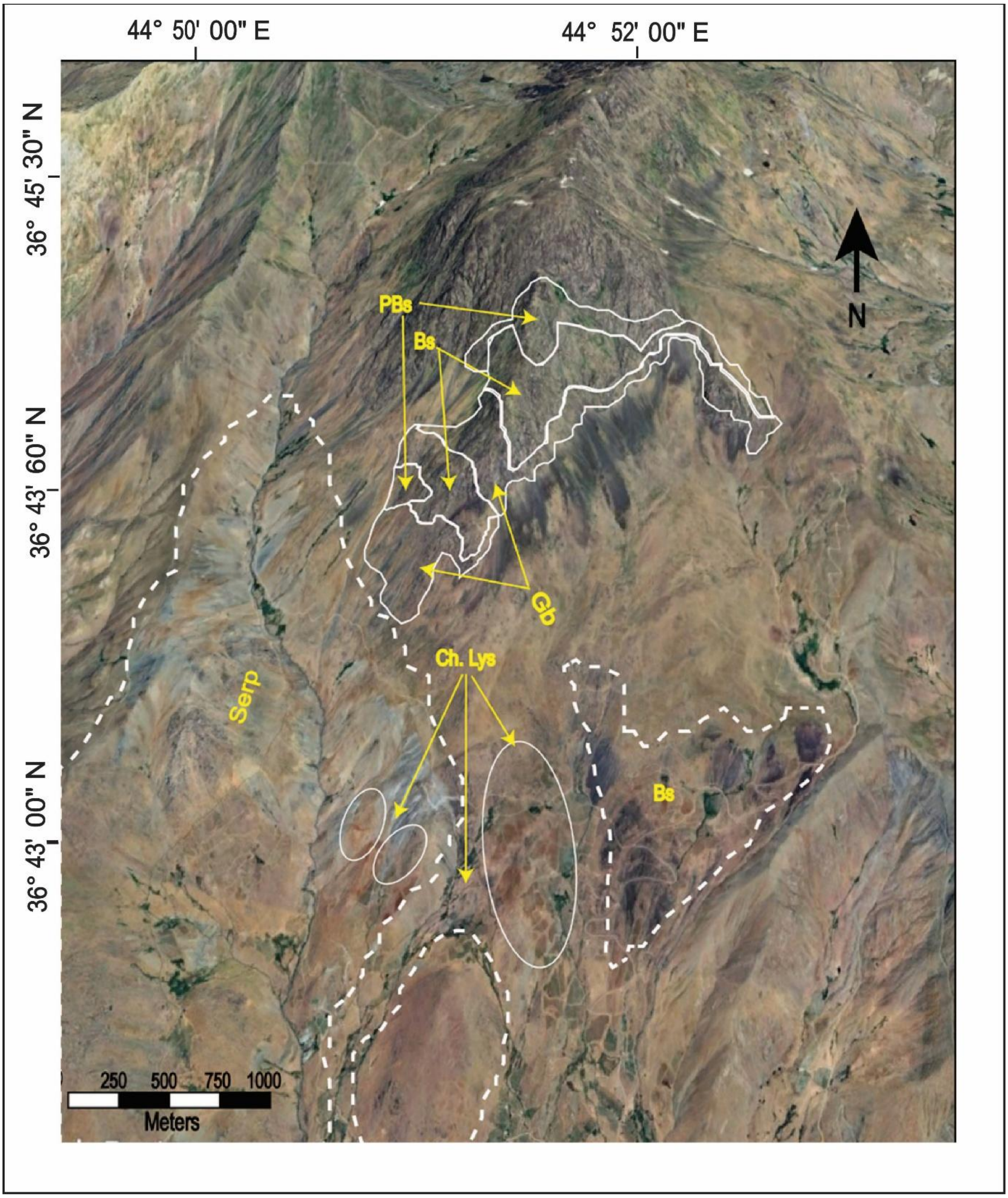

Figure 18. A Google map view displays the lithological units of Halgurd Mountain resembling an ophiolitic mélange in the study area (where Bs: basalt, Ch. Lys: chert layers, Serp: serpentinite, Gb: gabbro, PBs: pillow basalt).

The Hasanbag (106 – 92 Ma) and Walash-Naopurdan (43 – 24 Ma) arcs are located within the Penjween-Walash subzone. The initially inferred long gap between them (24 – 92 Ma), which might suggest spontaneous subduction initiation or dating uncertainties, is unlikely for Hassan bag – Halgord redion. Recent zircon U-Pb data date the Walash group to ~70 Ma (Mohammad et al., 2023), reducing the gap to about 70 – 92 Ma (S. A. Ali et al., 2012; Mohammad et al., 2023). Given that the typical lag between subduction initiation and arc volcanism is 5 – 15 million years (Stern, 2004). The Hassanbag-Halgurd arc–back-arc system aligns with a model of induced single subduction initiation during the Late Cretaceous. Therefore, the terminology for this arc–back-arc system should be reconsidered within the local geological framework and across Iraq more broadly. In addition, the geological map of the area requires revision and updating.

4.4. Slope, depth, and rate of cooling

The morphology, alignment, size, and shape of pillow basalts are commonly used to infer the slope on which lava was emplaced. Cylindrical, tube-like pillows elongated parallel to flow typically form on steep slopes, with slopes over 10° producing smaller, more elongated pillows (Umino et al., 2000; Walker, 1992b). Lava viscosity also affects pillow size; high-viscosity lava on steep slopes can still produce medium to large pillows *(Furnes & Fridleifsson, 1978)*.

The Halgurd Pillow Basalts (HPB) show diverse sizes and forms with sub-parallel elongation to flow direction, but some pillows exhibit re-entrant, curved, and overlapping shapes, indicating emplacement on a gentle slope. The variability in pillow size and shape may also result from multiple lava ascent stages, prolonged eruption, and sustained lava extrusion (Schnur, 2007). Vesicle type and distribution within pillows can indicate water depth during formation. Greater water depth reduces vesicle abundance, size, and density due to higher pressure preventing gas escape (Moore, 1965). The presence of pipe vesicles stretching from pillow centers outward and concentrated vesicles near pillow margins suggests formation at shallow depths, typically less than 350 – 450 m (Jones, 1970; Walker, 1992b). HPB contains numerous small, rounded, tubular, and spherical vesicles and amygdules densely concentrated at pillow margins, gradually decreasing in number but increasing in size toward the core. Pipe vesicles radiate from pillow centers toward rims, reflecting gas escape during cooling.

Cooling rate can be estimated from pillow rim thickness and inter-pillow material volume. Thin pillow margins indicate rapid cooling, while thicker rims reflect slower cooling (Dimroth et al., 1978). Abundant inter-pillow materials, which in HPB are yellow to pea-colored rinds 1 – 2 cm thick formed by chloritization (alteration from seawater interaction after outer shell fracturing), also suggest fast cooling *(Swanson & Schiffman, 1979; Ural, 2014; Walker, 1992b)*. The loose packing, visible inter-pillow spaces, and floating pillows within the matrix further support rapid cooling at relatively shallow water depth. The absence of large cavities within pillows likely reflects low volatile content in the lava.

4.5. Magmatic condition

The mineral composition of any igneous rock is greatly affected by the bulk composition of magma and magmatic condition factors such as water fugacity (fH2O), oxygen fugacity (fO2), and temperature. The formation of clinopyroxene and orthopyroxene in fresh basalt does not occur simultaneously; As a result, they are not subject to the same equilibrium conditions.

Geothermometer readings of *Nimis & Taylor (2000)* clinopyroxene indicate a temperature range of 628 to 875 °C. High pressure (5.2 kbar) at 875 °C (5.2 kbar), indicating a deeper level of intrusion, while when pressure is lower (1.6 kbar) at 628 °C, it is consistent with a shallower intrusion (Putirka, 2008). The graphical thermometer of Lindsley (1983) is used to estimate the equilibration temperature at which pyroxenes were crystallized. Based on the graphical thermometry of pyroxene varieties, the temperature of the analyzed clinopyroxenes is in the range of 600 – 800 °C isotherms (Figure 10b), indicating the crystallization of pyroxene after Ca-plagioclase and initiation of clinopyroxene equilibration at a deeper level prior to the eruption of melt on the surface. Oxygen fugacity is used as a valuable parameter in the evaluation of oxidation state in magmatic systems, and it plays an important role in the formation and stability of Fe-Ti bearing minerals during the equilibrium condition of the melt. The oxygen fugacity of the melt is normally achieved through using the mathematical solution *(Spencer & Lindsley, 1981)*. Hematite and magnetite are the two common oxide minerals in the HPB. However, due to the exposure of the area to the alteration processes, these phases are usually found with textures like amygdules and a brecciated zone. This indicates that their abundance may reflect secondary alterations rather than primary igneous processes. Thus, the estimation of oxygen fugacity (fO_2) based on the secondary oxides is unreliable.

5. Conclusion

The Halgurd Mountain represents a complete ophiolite sequence within the Iraqi Zagros ophiolite-bearing terrain along the Iran border. The Halgurd Pillow Basalts (HPB) display clear geochemical signatures of moderate Cr, Ni, and Ce/Yb ratios, indicating a magma source from partial melting of spinel-bearing peridotite with olivine, spinel, amphibole, and clinopyroxene fractionation. Morphological and vesicle features suggest lava emplacement on gentle slopes at relatively shallow water depth with rapid cooling. Tectonic discrimination diagrams reveal formation in a relatively deep back-arc basin, closely related to E-type MORB, with the effect of slab dehydration. This setting is part of the Iraqi Zagros Suture Zone’s arc–back-arc rift systems, specifically the Hasanbag–Halgurd and Walash-Naopurdan systems, formed during the Neo-Tethys opening (~106 – 50 Ma). Thermometry confirms that clinopyroxene and plagioclase equilibrated at depth prior to eruption, underscoring the region’s complex magmatic and tectonic evolution.

Authors’ Contributions

Author 1: Conceptualization, Software, methodology, investigation, writing, submission; Author 2: conceptualization, software, validation, investigation, revision, Supervision; Author 3: conceptualization, validation, investigation, revision, Supervision.

References

Abdulrehman, Z. S., Aqrawi, A. M., & Koshnaw, R. I. (2023). Characterization of the Govanda Formation limestones: chemostratigraphy and tectonic setting of the last marine carbonate rocks in the Arabia–Eurasia suture zone . *Carbonates and Evaporites*, *38*(4), 72. https://doi.org/10.1007/S13146-023-00897-3

Agard, P., Omrani, J., Jolivet, L., Whitechurch, H., Vrielynck, B., Spakman, W., Monié, P., Meyer, B., & Wortel, R. (2011). Zagros orogeny: a subduction-dominated process. *Geological Magazine*, *148*(5–6), 692–725. https://doi.org/10.1017/S001675681100046X

Ahmad, M., Paul, A. Q., & Saikia, A. (2024). Pillow Morphology of Bathani Volcano-sedimentary Sequence of Eastern Indian Shield: Inferences on the Geotectonic and Geo-Environments. *Journal of the Geological Society of India*, *100*(2), 218–232. https://doi.org/10.17491/JGSI/2024/173821

Alavi, M. (1994). Tectonics of the Zagros orogenic belt of Iran: new data and interpretations. *Tectonophysics*, *229*(3–4), 211–238. https://doi.org/10.1016/0040-1951(94)90030-2

Aldanmaz, E., Pearce, J. A., Thirlwall, M. F., & Mitchell, J. G. (2000). Petrogenetic evolution of late Cenozoic, post-collision volcanism in western Anatolia, Turkey. *Journal of Volcanology and Geothermal Research*, *102*(1–2), 67–95. https://doi.org/10.1016/S0377-0273(00)00182-7

Ali, S. A. (2012). Geochemistry and geochronology of Tethyan-arc related igneous rocks, NE Iraq [University of Wollongong]. In *ro.uow.edu.au*. https://ro.uow.edu.au/ndownloader/files/50371218/1

Ali, S. A., Buckman, S., Aswad, K. J., Jones, B. G., Ismail, S. A., & Nutman, A. P. (2012). Recognition of Late Cretaceous Hasanbag ophiolite-arc rocks in the Kurdistan Region of the Iraqi Zagros suture zone: A missing link in the paleogeography of the closing Neotethys Ocean. *Lithosphere*, *4*(5), 395–410. https://doi.org/10.1130/L207.1

Aswad, Buckman, S., Aswad, K. J., Jones, B. G., Ismail, S. A., & Nutman, A. P. (2013). The tectonic evolution of a Neo-Tethyan (Eocene–Oligocene) island-arc (Walash and Naopurdan groups) in the Kurdistan region of the Northeast Iraqi Zagros Suture Zone. *Island Arc*, *22*(1), 104–125. https://doi.org/10.1111/IAR.12007

Ali, S. A., Nutman, A. P., Aswad, K. J., & Jones, B. G. (2019). Overview of the tectonic evolution of the Iraqi Zagros thrust zone: Sixty million years of Neotethyan ocean subduction. *Journal of Geodynamics*, *129*, 162–177. https://doi.org/10.1016/J.JOG.2019.03.007

Ali, & Rostum, Z. (2021). Petrography and Geochemistry of Gabbroic Rock from the Penjwin Ophiolite, Kurdistan Region, Northeastern Iraq. *The Iraqi Geological Journal*, *2E*, 24–37. https://doi.org/10.46717/igj.54.2E.3Ms-2021-11-19

Al-Qayim, B., Omer, A., & Koyi, H. (2012). Tectonostratigraphic overview of the Zagros Suture Zone, Kurdistan Region, Northeast Iraq. *GeoArabia*, *17*(4), 109–156. https://doi.org/10.2113/GEOARABIA1704109

Aswad, K. J., Aziz, N. R., & Koyi, H. A. (2011). Cr-spinel compositions in serpentinites and their implications for the petrotectonic history of the Zagros Suture Zone, Kurdistan Region, Iraq. *Geological Magazine*, *148*(5–6), 802–818. https://www.cambridge.org/core/journals/geological-magazine/article/crspinel-compositions-in-serpentinites-and-their-implications-for-the-petrotectonic-history-of-the-zagros-suture-zone-kurdistan-region-iraq/544128B3AB8144376DC351E855CE8791

Aziz, N. R., Elias, E. M., & Aswad, K. J. (2011). RB-SR and SM-ND Isotopes Study of Serpentinites and their Impact on the Tectonic Setting of Zagros Suture Zone, NE Iraq. *Iraqi Bulletin of Geology and Mining*, *7*(1), 67–75. https://ibgm-iq.org/ibgm/index.php/ibgm/article/view/141

Azizi, H., Hadi, A., Asahara, Y., & Mohammad, Y. O. (2013). Geochemistry and geodynamics of the Mawat mafic complex in the Zagros Suture zone, northeast Iraq. *Central European Journal of Geosciences*, *5*(4), 523–537. https://doi.org/10.2478/S13533-012-0151-6

Boniface, N., & T Tsujimori. (2019). Pillow lava basalts with back-arc MORB affinity from the Usagaran Belt, Tanzania: relics of Orosirian ophiolites. *Geological Society*, *176*(5), 1007–1021. https://doi.org/10.1144/JGS2018-205

Buday, T. (1975). The two main structural units of the Tertiary eugeosyncline of Northeastern Iraq. *Jour. Geol. Soc. of Iraq, Spec Issue, Baghdad*.

Cann, J. R. (1970). Rb, Sr, Y, Zr, and Nb in some ocean floor basaltic rocks. *Earth and Planetary Science Letters*, *10*(1), 7–11. https://doi.org/10.1016/0012-821X(70)90058-0

Capan, U. Z., & Floyd, P. A. (1985). Geochemical and petrographic features of metabasalts within units of the Ankara Melange. *Ofioliti*, *10*(1), 3–12. https://pascal-francis.inist.fr/vibad/index.php?action=getRecordDetail&idt=8677341

Chadwick. Jr, W., & Embley, R. W. (1994). Lava flows from a mid-1980s submarine eruption on the Cleft segment, Juan de Fuca Ridge. *Journal of Geophysical Research: Solid Earth*, *99*(B3), 4761–4776. https://doi.org/10.1029/93JB02041

Chaib, L., Lahna, A. A., Admou, H., & Youbi, N. (2021). Geochemistry and geochronology of the Neoproterozoic Backarc basin Khzama ophiolite (Anti-Atlas Mountains, Morocco): Tectonomagmatic implications. *Minerals*. https://www.mdpi.com/2075-163X/11/1/56

Condie, K. C. (2005). High field strength element ratios in Archean basalts: a window to evolving sources of mantle plumes? *Lithos*, *79*(3–4), 491–504. https://doi.org/10.1016/J.LITHOS.2004.09.014

Deer, W. A., Howie, R. A., & Zussman, J. (2013). An Introduction to the Rock-Forming Minerals. In *An Introduction to the Rock-Forming Minerals*. Mineralogical Society of Great Britain and Ireland. https://doi.org/10.1180/DHZ

Dilek, Y., & Newcomb, S. (2003). Ophiolite concept and the evolution of geological thought. *Geological Society of America*, *373*. https://doi.org/10.1130/SPE373

Dimroth, E., Cousineau, P., Leduc, M., & Sanschagrin, Y. (1978). Structure and organization of Archean subaqueous basalt flows, Rouyn–Noranda area, Quebec, Canada. *Canadian Journal of Earth Sciences*, *15*(6), 902–918. https://doi.org/10.1139/E78-101

Duncan, R. A., Green, D. H., & 1987, undefined. (1987). The genesis of refractory melts in the formation of oceanic crust. *Contributions to Mineralogy and Petrology*, *96*(3), 326–342. https://doi.org/10.1007/BF00371252

Ellam, R. M. (1992). Lithospheric thickness as a control on basalt geochemistry. *Geology*, *20(2)*, 153–156. https://pubs.geoscienceworld.org/gsa/geology/article-abstract/20/2/153/205658

Farahmand, H., & Arian, M. A. (2014). Petrology and Petrogenesis of Mianrahan Pillow Lavas, Northeast of Kermanshah, West of Iran. *World Journal of Environmental Biosciences*, *6*, 43–49. www.environmentaljournals.org

Fink, J. H., & Griffiths, R. W. (1990). Radial spreading of viscous-gravity currents with solidifying crust. *Journal of Fluid Mechanics*, *221*, 485–509. https://doi.org/10.1017/S0022112090003640

Fouad. (2014). Western Zagros Fold – Thrust Belt, Part II: The High Folded Zone. *Iraqi Bulletin of Geology and Mining*, *6*, 53–71. https://ibgm-iq.org/ibgm/index.php/ibgm/article/view/275

Fouad, S. F. (2015). Tectonic map of Iraq, scale 1: 1000 000, 2012. *Iraqi Bulletin of Geology and Mining*, *11(1)*. https://ibgm-iq.org/ibgm/index.php/ibgm/article/view/262

Fretzdorff, S., Livermore, R. A., Devey, C. W., Leat, P. T., & Stoffers, P. (2002). Petrogenesis of the Back-arc East Scotia Ridge, South Atlantic Ocean. *Journal of Petrology*, *43*(8), 1435–1467. https://doi.org/10.1093/PETROLOGY/43.8.1435

Fridleifsson, I. B., Furnes, H., & Atkins, F. B. (1982). Subglacial volcanics — on the control of magma chemistry on pillow dimensions. *Journal of Volcanology and Geothermal Research*, *13*(1–2), 103–117. https://doi.org/10.1016/0377-0273(82)90022-1

Furnes, H., & Fridleifsson, I. B. (1978). Relationship between the chemistry and axial dimensions of some shallow water pillow lavas of alkaline olivine basalt and olivine tholeiitic composition. *Bulletin Volcanologique*, *41*(2), 136–146. https://doi.org/10.1007/BF02597027/METRICS

Gaetani, G. A., Kent, A. J. R., Grove, T. L., Hutcheon, I. D., & Stolper, E. M. (2003). Mineral/melt partitioning of trace elements during hydrous peridotite partial melting. *Contributions to Mineralogy and Petrology*, *145*(4), 391–405. https://doi.org/10.1007/S00410-003-0447-0/METRICS

Goff, J., & Jassim, S. (2006). Geology of Iraq. In *2006*. Czech Republic, Dolin, Prague and Moravian Museum, Brno.

Green, T. H. (1980). Island arc and continent-building magmatism — A review of petrogenic models based on experimental petrology and geochemistry. *Tectonophysics*, *63*(1–4), 367–385. https://doi.org/10.1016/0040-1951(80)90121-3

Griffiths, R. W., & Fink, J. H. (1992). Solidification and morphology of submarine lavas: A dependence on extrusion rate. *Journal of Geophysical Research: Solid Earth*, *97*(B13), 19729–19737. https://doi.org/10.1029/92JB01594

Guilmette, C., van Hinsbergen, D. J. J., Smit, M. A., Godet, A., Fournier-Roy, F., Butler, J. P., Maffione, M., Li, S., & Hodges, K. (2023). Formation of the Xigaze Metamorphic Sole under Tibetan continental lithosphere reveals generic characteristics of subduction initiation. *Communications Earth and Environment*, *4*(1), 1–10. https://doi.org/10.1038/S43247-023-01007-W;SUBJMETA

Hall, R. (2019). The subduction initiation stage of the Wilson cycle. *Geological Society Special Publication*, *470*(1), 415–437. https://doi.org/10.1144/SP470.3

Honza, E. (1991). The Tertiary Arc Chain in the Western Pacific. *Tectonophysics*, *187*(1–3), 285–303. https://doi.org/10.1016/0040-1951(91)90425-R

Humphris, S. E., & Thompson, G. (1978). Trace element mobility during hydrothermal alteration of oceanic basalts. *Geochimica et Cosmochimica Acta*, *42*(1), 127–136. https://doi.org/10.1016/0016-7037(78)90222-3

Ishizuka, H., Kawanobe, Y., & Sakai, H. (1990). Petrology and geochemistry of volcanic rocks dredged from the Okinawa Trough, an active back-arc basin. *Geochemical Journal*, *24*(2), 75–92. https://doi.org/10.2343/GEOCHEMJ.24.75

Jones, J. G. (1970). Intraglacial volcanoes of the Laugarvatn region, southwest Iceland, II. *Quarterly Journal of the Geological Society*, *124(1-4)*(2), 197–211. https://doi.org/10.1086/627496

Juteau, T. (1993). Le volcanisme des dorsales océaniques. *Mémoires de La Société Géologique de France (1833)*, *163*, 81–98.

Kennish, M. J., & Lutz, R. A. (1998). Morphology and distribution of lava flows on mid-ocean ridges: a review. *Earth-Science Reviews*, *43*(3–4), 63–90. https://doi.org/10.1016/S0012-8252(98)00006-3

Koshnaw, R. I., Stockli, D. F., & Schlunegger, F. (2019). Timing of the Arabia-Eurasia continental collision—Evidence from detrital zircon U-Pb geochronology of the Red Bed Series strata of the northwest Zagros hinterland, Kurdistan region of Iraq. *Geology*, *47*(1), 47–50. https://doi.org/10.1130/G45499.1

Kuibida, M. L. (2019). Basaltic Volcanism of Island-Arc–Back-Arc Basin System (Altai Active Margin). *Russian Journal of Pacific Geology*, *13*(3), 297–309. https://doi.org/10.1134/S1819714019030059/METRICS

Lambert, R. S. J., Holland, J. G., & Owen, P. F. (1974). Chemical Petrology of a Suite of Calc-Alkaline Lavas from Mount Ararat, Turkey. *The Journal of Geology*, *82*(4), 419–438. https://doi.org/10.1086/627992

Langdon, G. S. (1982). *The petrology, geochemistry, and petrogenesis of the upper pillow lavas, Troodos Ophiolite Complex, Cyprus* [University of Newfoundland]. https://hdl.handle.net/20.500.14783/3096

Lawa, F. A., Koyi, H., & Ibrahim, A. (2013). Tectono-Stratigraphic Evolution of the NW Segment of the Zagros Fold-Thrust Belt, Kurdistan, NE IRAQ. *Journal of Petroleum Geology*, *36*(1), 75–96. https://doi.org/10.1111/JPG.12543

Le Bas, M. J. (1986). A chemical classification of volcanic rocks based on the total alkali-silica system. *J. Petrol*, *27*, 247–257. https://cir.nii.ac.jp/crid/1570572699163927296

Lindsley, D. H. (1983). Pyroxene thermometry. *American Mineralogist*, *68*, 447–493. https://pubs.geoscienceworld.org/msa/ammin/article-abstract/68/5-6/477/104808

Mackay-Champion, T. C., Searle, M. P., Tapster, S., Roberts, N. M. W., Shail, R. K., Palin, R. M., Willment, G. H., & Evans, J. T. (2024). Magmatic, Metamorphic and Structural History of the Variscan Lizard Ophiolite and Metamorphic Sole, Cornwall, UK. *Tectonics*, *43*(4), e2023TC008187. https://doi.org/10.1029/2023TC008187

Manikyamba, C., & Kerrich, R. (2011). Geochemistry of alkaline basalts and associated high-Mg basalts from the 2.7 Ga Penakacherla Terrane, Dharwar craton, India: An Archean depleted mantle-OIB array. *Precambrian Research*, *188*(1–4), 104–122. https://doi.org/10.1016/J.PRECAMRES.2011.03.013

Martí, J., Martí, J., & Ernst, G. (2005). Volcanoes and the Environment. In *Cambridge University Press*.

Mckenzie, D., & O'nions, R. K. (1991). Partial Melt Distributions from Inversion of Rare Earth Element Concentrations. *Journal of Petrology*, *32*(5), 1021–1091. https://doi.org/10.1093/PETROLOGY/32.5.1021

Moghadam, H. S., Corfu, F., Stern, R. J., & Bakhsh, A. L. (2019). The Eastern Khoy metamorphic complex of NW Iran: A Jurassic ophiolite or continuation of the Sanandaj-Sirjan zone? *Journal of the Geological Society*, *176*(3), 517–529. https://doi.org/10.1144/JGS2018-081

Moghadam, H. S., Li, Q. L., Stern, R. J., Chiaradia, M., Karsli, O., & Rahimzadeh, B. (2020). The Paleogene ophiolite conundrum of the Iran–Iraq border region. *Journal of the Geological Society*, *177*(5), 955–964. https://doi.org/10.1144/JGS2020-009

Mohammad, Abdulla, K., & Azizi, H. (2023). Late Cretaceous-Paleocene Arc and Back-Arc System in the Neotethys Ocean, Zagros Suture Zone. *Minerals*, *13(11)*, 1367. https://www.mdpi.com/2075-163X/13/11/1367

Mohammad, & Cornell, D. H. (2017). U–U-Pb zircon geochronology of the Daraban leucogranite, Mawat ophiolite, Northeastern Iraq: a record of the subduction to collision history for the Arabia–Eurasia plates. *Island Arc*, *26*(3), e12188. https://doi.org/10.1111/IAR.12188

Mohammad, Cornell, D. H., Qaradaghi, J. H., & Mohammad, F. O. (2014). Geochemistry and Ar–Ar muscovite ages of the Daraban Leucogranite, Mawat Ophiolite, northeastern Iraq: implications for Arabia–Eurasia continental collision. *Journal of Asian Earth Sciences*, *86*, 151–165. https://doi.org/10.1016/j.jseaes.2013.09.029

Moore, J. J. (1965). Petrology of deep-sea basalt near Hawaii. *Amer. Jour. Sci*, *263*, 40–52. https://cir.nii.ac.jp/crid/1570291225191987328

Morimoto, N. (1988). Nomenclature of pyroxenes. *Mineralogy and Petrology*, *39(1)*, 55–76. http://rruff.geo.arizona.edu/doclib/mm/vol52/MM52_535.pdf

Mouthereau, F., Lacombe, O., & Verges, J. (2012). Building the Zagros collisional orogen: timing, strain distribution, and the dynamics of Arabia/Eurasia plate convergence. *Tectonophysics*, *532*, 27–60. https://doi.org/10.1016/j.tecto.2012.01.022

Nimis, P., & Taylor, W. R. (2000). Single clinopyroxene thermobarometry for garnet peridotites. Part I. Calibration and testing of a Cr-in-Cpx barometer and an enstatite-in-Cpx thermometer. *Contributions to Mineralogy and Petrology*, *139*(5), 541–554. https://doi.org/10.1007/S004100000156/METRICS

Othman, A. A., & Gloaguen, R. (2013). Automatic Extraction and Size Distribution of Landslides in Kurdistan Region, NE Iraq. *Remote Sensing 2013, Vol. 5, Pages 2389-2410*, *5*(5), 2389–2410. https://doi.org/10.3390/RS5052389

Pearce, J. A. (2008). Geochemical fingerprinting of oceanic basalts with applications to ophiolite classification and the search for Archean oceanic crust. *Lithos*, *100*(1–4), 14–48. https://doi.org/10.1016/J.LITHOS.2007.06.016

Putirka, K. D. (2008). Thermometers and Barometers for Volcanic Systems. *Reviews in Mineralogy and Geochemistry*, *69*(1), 61–120. https://doi.org/10.2138/RMG.2008.69.3

Qaradaghi, J. M., Mohammed, Y. O., & Aziz, S. A. (2019). Petrology and Geochemistry of Gole Pillow Basalt in Penjween area, Kurdistan Region, NE Iraq. *Tikrit Journal of Pure Science*, *24*(7), 66–81. https://doi.org/10.25130/tjps.24.2019.131

Ramsay, W. R. H., & Moore, P. R. (1985). Mineralogy and chemistry of a pillow lava, Northland, New Zealand, and its tectonic significance. *New Zealand Journal of Geology and Geophysics*, *28*(3), 471–485. https://doi.org/10.1080/00288306.1985.10421200

RL, R. (2005). Composition of the continental crust. *The Crust, Treatise on Geochemistry*, *3*, 17–18. https://doi.org/10.15080/AGCJCHIKYUKAGAKU.66.5_163

Schnur, S. R. (2007). *An analysis of the morphology and physical properties of Pillow Lavas of the Nicasio Reservoir Terrane, Marin County, California: implications for seamount formation and structure*. Carleton College.

Shervais, J. W. (1982). Ti-V plots and the petrogenesis of modern and ophiolitic lavas. *Earth and Planetary Science Letters*, *59*(1), 101–118. https://doi.org/10.1016/0012-821X(82)90120-0

Sissakian, V. K. (2013). Geological evolution of the Iraqi Mesopotamia Foredeep, inner platform, and near surroundings of the Arabian Plate. *Journal of Asian Earth Sciences*, *72*, 152–163. https://doi.org/10.1016/J.JSEAES.2012.09.032

Spencer, K. J., & Lindsley, D. H. (1981). A solution model for coexisting iron–titanium oxides. *American Mineralogist*, *66(11-12)*, 1189–1201. https://pubs.geoscienceworld.org/msa/ammin/article-abstract/66/11-12/1189/41238/A-solution-model-for-coexisting-iron-titanium

Stern, R. J. (2004). Subduction initiation: spontaneous and induced. *Earth and Planetary Science Letters*, *226*(3–4), 275–292. https://doi.org/10.1016/J.EPSL.2004.08.007

Stern, R. J., & Gerya, T. (2018). Subduction initiation in nature and models: A review. *Tectonophysics*, *746*, 173–198. https://doi.org/10.1016/J.TECTO.2017.10.014

Sun, S. S., & McDonough, W. F. (1989). Chemical and isotopic systematics of oceanic basalts: Implications for mantle composition and processes. *Geological Society Special Publication*, *42*(1), 313–345. https://doi.org/10.1144/GSL.SP.1989.042.01.19

Swanson, S. E., & Schiffman, P. (1979). Textural evolution and metamorphism of pillow basalts from the Franciscan Complex, western Marin County, California. *Contributions to Mineralogy and Petrology*, *69*(3), 291–299. https://doi.org/10.1007/BF00372331/METRICS

Tong, Z., Ding, W., Wang, C., & Li, C. F. (2024). Analogue modelling of subduction initiation: a review and perspectives. *International Geology Review, 66(11)*, 2123–2165. https://doi.org/10.1080/00206814.2023.2272273

Tronnes, R. (2002). "Geology and geodynamics of Iceland: In *Nordic Volcanological Institute* (Vols. 1–19). University of Iceland.

Umino, S., Lipman, P., & Obata, S. (2000). Subaqueous lava flow lobes, observed on ROV KAIKO dives off Hawaii. *Geology*, *28(6)*, 503–506. https://pubs.geoscienceworld.org/gsa/geology/article-abstract/28/6/503/185688

Ural, M. (2014). Morphologic and physical features of pillow basalts of the Yüksekova Complex around Elazığ (Eastern Anatolia, Turkey). *Quarterly Journal of Tethys*, *2*(1), 70–80. https://jtethys.journals.pnu.ac.ir/article_2816.html

Ural, M., Arslan, M., Göncüoglu, M., Tekin, K., & Ofioliti, S. K.-. (2015). Late Cretaceous arc and back-arc formation within the Southern Neotethys: whole-rock, trace element and Sr-Nd-Pb isotopic data from basaltic rocks of the Yüksekova. *Ofioliti.*, *40(1)*. https://www.ofioliti.it/index.php/ofioliti/article/view/435

Van Hinsbergen, D. J. J., Peters, K., Maffione, M., Spakman, W., Guilmette, C., Thieulot, C., Plümper, O., Gürer, D., Brouwer, F. M., Aldanmaz, E., & Kaymakci, N. (2015). Dynamics of intraoceanic subduction initiation: 2. Suprasubduction zone ophiolite formation and metamorphic sole exhumation in context of absolute plate motions. *Geochemistry, Geophysics, Geosystems*, *16*(6), 1771–1785. https://doi.org/10.1002/2015GC005745

Walker, G. P. L. (1992a). Morphometric study of pillow-size spectrum among pillow lavas. *Bulletin of Volcanology*, *54*(6), 459–474. https://doi.org/10.1007/BF00301392/METRICS

Walker, G. P. L. (1992b). Morphometric study of pillow-size spectrum among pillow lavas. *Bulletin of Volcanology*, *54*(6), 459–474. https://doi.org/10.1007/BF00301392/METRICS

Winchester, J. A., & Floyd, P. A. (1977). Geochemical discrimination of different magma series and their differentiation products using immobile elements. *Chemical Geology*, *20*(C), 325–343. https://doi.org/10.1016/0009-2541(77)90057-2

Winter, J. D. (John D. (2010). An introduction to igneous and metamorphic petrology. In *(No Title)*. Prentice Hall, 2nd ed., International ed. https://cir.nii.ac.jp/crid/1971149384787867077

Xia, L., & Li, X. (2019). Basalt geochemistry as a diagnostic indicator of tectonic setting. *Gondwana Research*, *65*, 43–67. https://doi.org/10.1016/J.GR.2018.08.006

Xia, L. Q., Li, X. M., Yu, J. Y., & Wang, G. Q. (2016). Mid-late Neoproterozoic to early Paleozoic volcanism and tectonic evolution of the Qilianshan, NW China. *GeoResJ*, *9–12*, 1–41. https://doi.org/10.1016/J.GRJ.2016.06.001

Zhou, X., & Wada, I. (2021). Differentiating induced versus spontaneous subduction initiation using thermomechanical models and metamorphic soles. *Nature Communications*, *12*(1), 1–10. https://doi.org/10.1038/S41467-021-24896-X;SUBJMETA